UNIVERSITY OF OULU

Spectroscopic shifts as a signature of many-body localization phase transition in a one-dimensional transmon array

Master's Thesis

by

Sasu Tuohino

Faculty of Science
Nano and Molecular Systems Research Unit
Theoretical physics

September 2019

Abstract

Many-body localization is a phase of matter, which can occur in systems with strong disorder and interactions. One of the main characteristics of the many-body localized phase is that it cannot thermalize because localization slows or stops the propagation of information inside the system. Here, we study many-body localization in a one-dimensional transmon qubit array theoretically and numerically. Differing from frequently used approaches to many-body localization, we study the dynamical phase transition between a thermalized phase and the many-body localized phase by using a numerical method that is based on Fermi's golden rule. This method makes it possible to distinguish the thermalized phase from the many-body localized phase and allows one to estimate how much disorder is required for the many-body localization phase transition. The distinction between the phases is made by a "soft" gap which appears at the zero-frequency and is known as a universal sign of localization. Unlike many other methods, which are used to recognize the many-body localized phase, the method in question can be easily applied to experiments. In the system that we have chosen the transmon qubits are capacitively coupled to each other, and the system is driven by a harmonic external magnetic flux that induces transitions between the energy eigenstates of the system.

We calculated the numerical results for a system with eight transmon qubits, and to make calculations simpler, we assumed that the temperature of the system is infinite. The size of the system is limited by the computational expensiveness of our method. Somewhat surprisingly, the most laborious part of the calculations proved to be the Fermi's golden rule, which is used to calculate the transition rate spectrum.

The results show that the method in question can distinguish the many-body localized phase if the strength of disorder in the system is large, but near the many-body localized phase transition, it is challenging to observe the difference between the thermalized phase and the many-body localized phase. We calculated the transition rate spectra using different values of on-site interaction strength. The results show us that the disorder strength needed for the phase transition is smaller if the on-site interaction strength is weak or very strong. Lastly, we demonstrated the many-body localization phase transition by calculating the energy eigenstates as a function of disorder strength and observing how strongly the eigenenergies repel each other. This method proved to be relatively imprecise to specify the critical disorder strength needed for the many-body localized phase. However, one can clearly notice that the repulsion between energy levels grows weaker as the disorder strength grows stronger.

Contents

Abstract i

1 Introduction 1

2 What is localization? 3
2.1 Thermalization . . . 4
2.1.1 Isolated quantum systems . . . 4
2.1.2 Eigenstate thermalization hypothesis . . . 5
2.1.3 Paradox of quantum thermalization . . . 6
2.2 Different types of localization . . . 7
2.2.1 Anderson localization . . . 8
2.2.2 Many-body localization . . . 9
2.3 Signatures of many-body localization . . . 11
2.3.1 Emergent integrability . . . 11
2.3.2 Logarithmic growth of entanglement . . . 14
2.3.3 Dephasing dynamics of quasi-local operators . . . 17
2.3.4 Area-law entanglement in MBL eigenstates . . . 18

3 Reflection spectroscopy and Fermi's golden rule 20
3.1 Spectral diagnostics of many-body localization . . . 21
3.1.1 Interpretation of the spectral function . . . 22
3.1.2 Spectral function at zero-coupling limit and for temperature T . . . 23
3.1.3 How interactions affect the spectral function? . . . 24
3.1.4 Weak and strong regimes of MBL . . . 25
3.1.5 Strong-weak MBL transition in finite temperature . . . 27
3.1.6 The universal characteristic of localization . . . 28
3.1.7 The role of dissipation . . . 31
3.1.8 What about probes coupled to physical spins? . . . 32
3.2 Fermi's golden rule . . . 32
3.2.1 Derivation . . . 32
3.2.2 Connection between absorption spectrum and transition rates . . . 35

4 Physical setup: 1-D transmon array and Bose-Hubbard model 37
4.1 Bose-Hubbard model . . . 37
4.2 Transmon qubit . . . 38
4.2.1 Derivation of 1-D transmon array Hamiltonian . . . 39
4.2.2 Quantum picture . . . 43

4.2.3 Connection to Bose-Hubbard model 44
4.2.4 Driving transmon with magnetic flux 46
4.2.5 Transmon Hamiltonian with magnetic flux drive 48
4.2.6 Implementing disorder with magnetic flux 49
4.3 Fermi's golden rule for harmonic magnetic flux perturbation 50

5 Numerical methods and efficiency **51**

6 Results & Discussion **53**
6.1 Transition rate spectra 53
6.1.1 Changing the strength of the disorder 53
6.1.2 Changing the strength of the on-site interaction 56
6.2 Disorder sweep 61

7 Conclusions **64**

Chapter 1

Introduction

In the beginning of the 20$^{\text{th}}$-century, the first discoveries regarding the quantum nature of the reality were made, as Max Planck made his quantum hypothesis. A few years later, Albert Einstein published his paper on photoelectric effect, in which the nature of light is argued to be consistent with Planck's quantum hypothesis. In the early 1920s, the quantum theory started to develop into its more formal form, which is the theory of quantum mechanics we know today.

Quickly, the development of the quantum theory spawned some other fields of study related to quantum mechanics, like many-body quantum physics and condensed matter physics. These fields focus on the behaviour of large quantum systems, including many interacting particles (e.g. superconductivity). Many-body localization is an example of such collective phenomenon, present only in systems with many interacting particles.

One central character in the history of many-body localization is P. W. Anderson who is the pioneer of the studies regarding disorder-induced localization. In 1958, Anderson studied disorder-induced localization without interactions between particles [1]. This phenomenon was named after him as Anderson localization. Anderson also suggested that the localization might survive even if the interactions between particles are present, which is the first proposal for the existence of many-body localization. However, many-body localization did not attract much attention until 2005 (see Refs. [2–4]), but since then many-body localization has been a subject to much development and interest.

In the early 1980s, an interesting idea was proposed by Richard Feynman. He suggested that the most efficient way of computationally simulating the real-world physical systems is not with classical computation, but instead with quantum computation [5]. Since every real-world system is fundamentally quantum mechanical by its nature, it makes sense

that the accurate way to simulate any real-world system is to use a computer which operates using the quantum principles. Such device is called a quantum computer.

After Feynman made the concept of quantum computation popular, there has been some development regarding quantum algorithms, but the main problem lies in the physical realization of quantum computers. The issue which makes quantum computation difficult is the fragile nature of quantum states in the presence of environmental noise. Fortunately, there has been progress in the development of quantum systems, which are applicable for quantum computers. One such system is constructed by using superconductive quantum circuits. The first superconductive qubits were built in the late 1990s, but the superconductive designs for quantum computers gained more popularity in the late 2000s.

In this thesis, the research of many-body localization and superconducting qubits come together as we study the many-body localized phase transition in a 1-dimensional system made of superconducting qubits coupled to each other. Even though many-body localization has been a topic of much interest in recent years, there are not many articles which study it in superconducting qubits (there are few exceptions e.g. Ref. [6]).

In general, the motivation for the thesis is to study the spectroscopic approach to many-body localization by using the Fermi's golden rule in a one-dimensional transmon array, and see if it is a valid method to observe the phase transition from thermalized phase to many-body localized phase. Also, it is interesting to see if there are any significant differences compared to similar spectroscopic methods used in fermionic systems.

The thesis is organized in the following way: In chapter 2, we introduce some basic concepts regarding many-body localization (and also Anderson localization and thermalization). In chapter 3 we introduce the spectroscopic methods which are used to observe the phase transition between thermalized phase and many-body localized phase. In chapter 4 we focus on the mathematical formalism required for superconductive qubits. We also show the equivalence between the Hamiltonian describing the 1-D transmon qubit array and that of the widely-known Bose-Hubbard Hamiltonian. In chapter 5, we briefly discuss the numerical aspects of this thesis. The chapter 6 is preserved for the numerical results and for interpretation of these results. Finally, the thesis is concluded with the chapter 7, in which we summarise the most important aspects of the thesis.

Chapter 2

What is localization?

The term localization can refer to several different phenomena, but those considered in this thesis are related to *Anderson localization* and *many-body localization* (MBL). Anderson localization is not the main focus of this thesis, but due to many similarities with MBL, we go through the basics and use it as a stepping stone as we cover the more complicated problem of MBL. It is also useful to highlight the differences between these two types of localization.

In his work [1], Anderson considered a spin-lattice with a random element attached to its potential. He argued that the randomness of the potential will ultimately cause the system to localize, i.e. diffusive transport in the spatial dimensions vanishes and, in general, it is not dependent on the initial state of the system. For example, this could happen for a spin or an electron in a lattice, which is initialized into some non-equilibrium state. In such case, the vanishing transport of spins or electrons prevents the system from reaching the equilibrium. This phenomenon is not limited by the energy of the system and, therefore, it happens even in the situation where surrounding potentials are not large enough to confine the particle inside a restricted spatial region. The reason behind the localization is matter wave interference inflicted by the wave scattering from the random potential. This means that for particles (e.g. electrons) the Anderson localization is purely quantum mechanical phenomenon, but it can occur in the case of classical waves [7].

As pointed out, the disorder of the system (i.e. randomness in a potential) plays a fundamental role in creating the localization, but the disorder is not just an artificial assumption to create elegant physics. As a matter of fact, the nature is mostly comprised of disordered systems, since even though atoms and molecules of the same species are not separable, in large systems there are always e.g. impurities which play the role of disorder. Although it is easy to implement disorder to system, the localized phase is

sensitive towards coupling to external thermal reservoirs. For example, lattice vibrations can dissolve the coherent interferences of the matter waves and restore the diffusive transport of the system.

2.1 Thermalization

In the recent 150 years, statistical mechanics has proved its value in describing the behaviour of systems with a large number of degrees of freedom. This success can be confidently attributed to statistical ensembles (e.g. canonical ensemble, grand canonical ensemble) [8]. However, the usefulness of these ensembles is dependent on a crucial assumption: *Thermalization*. It describes a process where non-equilibrium initial state reaches thermal equilibrium with itself after some sufficiently long period of time. Reaching thermal equilibrium with itself means that if we consider any possible partition to subsystems these subsystems are in thermal equilibrium with each other. This holds also for states initially in thermal equilibrium, but that case is trivial and therefore not interesting.

In classical mechanics, one can describe the thermalization process by using the ergodicity hypothesis. It states that after sufficiently long time period the system will spend equal amount of time in every accessible and equally-sized region of the phase space. This is expressed by the equation [9–11]

$$\lim_{T\to\infty} \frac{1}{T} \int_0^T \mathcal{O}(q(t), p(t))dt = \frac{\int \mathcal{O}(q,p)\varrho(q,p)d^{3N}qd^{3N}p}{\int \varrho(q,p)d^{3N}qd^{3N}p}, \tag{2.1}$$

where the left hand side describes time average and right hand side is the average over whole accessible phase space in equilibrium for some physical quantity $\mathcal{O}$. This implicates that after long enough time the system as a whole will be described by microcanonical ensemble, and every finite subsystem follows canonical ensemble if the size of the complete system approaches the thermodynamic limit. The definition of ergodicity described above is applicable for classical systems, but applying the ergodic hypothesis to quantum mechanical systems is not as straightforward as one might naively think. The reason for these complications is the linearity of quantum mechanics [12].

2.1.1 Isolated quantum systems

Traditional way to justify the thermalization is to couple the system to an external reservoir, which ultimately thermalizes the system. But what happens if we decide to treat the small system and the external reservoir as a one big system? If one applies

the quantum formalism to this system, there is a Hamiltonian $\hat{H}$ that describes the time-evolution of the system. By assuming that the system is prepared to some generic non-equilibrium initial state $|\Psi(0)\rangle$, one can try to determine the conditions needed for thermalization. This state can be decomposed by using energy eigenstates $|\alpha\rangle$, and the time-evolution of the initial state takes the form [13]

$$|\Psi(t)\rangle = e^{-i\hat{H}t}\,|\Psi(0)\rangle = \sum_{\alpha} A_\alpha e^{-iE_\alpha t}\,|\alpha\rangle\,, \tag{2.2}$$

where E_α is the eigenenergy corresponding to eigenstate $|\alpha\rangle$. Also we have assumed that $\hbar = 1$. If the energy of the system is measured, each eigenstate is found with time-independent probability, $p_\alpha = \left|\langle\alpha|\Psi(t)\rangle\right|^2 = |A_\alpha|^2$, i.e. contrary to the classical counterpart, the system does not explore the whole phase space under unitary time-evolution [12]. However, by keeping in mind the intuitive interpretation of classical ergodicity, which is that after long enough time the expectation values of physical quantities are the same as one would expect for a system obeying microcanonical ensemble, one can adjust the classical ergodicity to fit into the quantum picture. Let $\hat{\mathcal{O}}$ be an operator that describes some physical quantity, and let non-equilibrium initial state be as in equation (2.2). Here the infinite-time average is

$$\begin{aligned}\langle\hat{\mathcal{O}}\rangle_\infty &= \lim_{T\to\infty}\frac{1}{T}\int_0^T \langle\Psi(t)|\hat{\mathcal{O}}|\Psi(t)\rangle\,dt \\ &= \lim_{T\to\infty}\frac{1}{T}\sum_{\alpha,\beta} A_\alpha A_\beta^* \int_0^T e^{-i(E_\alpha - E_\beta)t}\,\langle\beta|\hat{\mathcal{O}}|\alpha\rangle\,dt = \sum_\alpha p_\alpha\,\langle\alpha|\hat{\mathcal{O}}|\alpha\rangle\,,\end{aligned} \tag{2.3}$$

where the last equality follows from the fact that terms with oscillating time dependence average out as $T \to \infty$, i.e. the terms where $E_\alpha \neq E_\beta$ vanish [12, 14]. To make this compatible with the classical version of ergodicity one needs an assumption that is often referred as *eigenstate thermalization hypothesis*.

2.1.2 Eigenstate thermalization hypothesis

Ergodic hypothesis says that $\langle\hat{\mathcal{O}}\rangle_\infty \approx \langle\hat{\mathcal{O}}\rangle_{\text{mc}}(E)$, where the right hand side is expectation value for microcanonical ensemble around energy $E = E_\alpha$. In quantum mechanics, the microcanonical ensemble is described by such statistical distribution of quantum states that every energy eigenstate with energy, that is equal to the energy of the system, has the same probability, and for other eigenstates the probability is zero. One way to make quantum system fulfil this condition is to assume that expectation values of the observable $\hat{\mathcal{O}}$ for every energy eigenstate is the same as expectation value for microcanonical ensemble, i.e. $\langle\alpha|\hat{\mathcal{O}}|\alpha\rangle \approx \langle\hat{\mathcal{O}}\rangle_{\text{mc}}(E)$. This assumption was proposed in references [15, 16], and it is called eigenstate thermalization hypothesis (ETH). It is

still unclear if the ETH is a mandatory condition for thermalization, but it seems to be the case at least for all known systems [17]. Alternative short and comprehensive introduction to quantum thermalization and ETH is found in Ref. [18].

The concept of ETH is important also when studying localization, since one of the defining properties of localization is that the ETH does not hold. The system is fully localized if all eigenstates of the system break the ETH, and partially localized if some eigenstates violate ETH.

2.1.3 Paradox of quantum thermalization

At this point one might still wonder: How is it that a well-known nonequilibrium initial state, after unitary time-evolution, will end up to a thermal equilibrium state that is fully described by only few conserved quantities (e.g. temperature). The loss of information about the initial state seems to be contradicting the fact that the system is evolving under its own unitary dynamics, which means that the information concerning the initial state must be preserved. This is known as the paradox of quantum thermalization. The solution for this paradox is that the information concerning the local features of the initial state is extended over the whole system by entanglement. This means that the initial information, that could be easily measured with local operators in the beginning, is now hidden into global operators of the system, and the measurements of these global operators are practically impossible. This means that the local information (e.g. value of some individual spin) regarding the initial state is not lost, but it has spread over the whole system. In theory, this information still exists and should retrievable but is practically very hard or maybe even impossible to obtain [18].

Another way to look at this problem is to define small subsystem A where the interesting initial information is located and treat the rest of the system as an environment which acts on the subsystem A. In this case, the rest of the system acts as a reservoir for the subsystem A, and causes it to thermalize [18]. It is important to note that if we are tracking only the state ϱ_{A} then the dynamics are no longer unitary, and thus, it is not expected that the information regarding initial state will exist in the state ϱ_{A} as the subsystem A evolves over time

This source of thermalization is known as decoherence, and it is the main reason why application of quantum information are so difficult to realize. This clarifies one of the main reasons why localization and especially MBL has much interest in the field of quantum information. If the system is in MBL or Anderson localized phase the system will not be thermalized, and the information concerning the local properties of the initial

is preserved in a form that is accessible to local operators. Thus MBL system could be used as a "quantum memory" [18, 19].

2.2 Different types of localization

In the earlier section, we discussed about the thermalization, and presented an explanation why it is not possible to retrieve the information regarding the initial state after a sufficiently long time periods if the system occupies the thermalizing phase. Now we turn our focus to systems which do not thermalize, and occupy a localized phase instead. Our discussion will be limited to a localized phases that are induced by quenched disorder (i.e. static randomness) in on-site potential.

Most of the theoretical and numerical research on MBL is done by using one-dimensional model of spinless fermions or one-dimensional model of Heisenberg spins, and both of these models have only nearest-neighbour hopping interactions and on-site interactions. The disordered fermion model is described by the Hamiltonian

$$\hat{H} = \sum_i \epsilon_i \hat{n}_i + V \sum_i \hat{n}_i \hat{n}_{i+1} + J \sum_i (\hat{c}_i^\dagger \hat{c}_{i+1} + \hat{c}_{i+1}^\dagger \hat{c}_i), \tag{2.4}$$

where $\hat{n}_i$ and $\hat{c}_i^\dagger$ are the number operator and creation operator for site i, V is the interaction strength between adjacent fermions, J is the hopping interaction strength between neighbouring sites. On-site potential is defined as $\epsilon_i = \epsilon_0 + \frac{W}{2}[-1, 1]$ where $[-1, 1]$ gives some random number from unitary distribution defined between values -1 and 1. The parameter W defines the disorder strength. The model describing interacting spins is also known as random field XXZ spin chain, and Hamiltonian has the form

$$\hat{H}_{\mathrm{XXZ}} = \sum_i h_i \hat{\sigma}_i^z + J_z \sum_i \hat{\sigma}_i^z \hat{\sigma}_{i+1}^z + J_\perp \sum_i (\hat{\sigma}_i^x \hat{\sigma}_{i+1}^x + \hat{\sigma}_i^y \hat{\sigma}_{i+1}^y), \tag{2.5}$$

where $\boldsymbol{\sigma} = (\hat{\sigma}^x, \hat{\sigma}^y, \hat{\sigma}^z)$ are the $\frac{1}{2}$-spin operators, and the parameters in each term have the same interpretation as in Hamiltonian (2.4). The models of Eqs. (2.4) and (2.5) resemble each other and, in fact, the random field XXZ model can be mapped to the spinless fermion model by using the Jordan-Wigner transformation [12].

Here, we use these models to point out the generic characteristics of MBL phase even though the main results of this thesis are concerning a different bosonic model, known as the Bose-Hubbard model. However, the discussed properties of MBL phase are universal in this regard, and are present in some form regardless of the specific model that is used.

2.2.1 Anderson localization

Anderson localization is characterized by disorder-induced localization and absence of interactions between particles. Non-interacting particles are the reason why it is some times called single-particle localization, highlighting the difference compared to many-body localization. Because of the non-interacting particles, the basic idea behind localization is easier to understand in the case of Anderson localization.

For example, we initialize a system, that is described by the Hamiltonian (2.5) in Anderson localized phase, into a state which has only one excited spin. After arbitrarily long time period, the spatial wave function $\psi(x)$ is still centred around the initially excited spin. To be more specific, the maximum of the wave function is located at the site of initially excited spin, and the amplitude of the wave function decays exponentially as the distance from initially excited spin grows. This clearly contrasts the behaviour of the thermalizing phase, in which the wave function will be equally distributed over every spin in the system after a sufficiently long time period has passed.

In systems with spatial dimensions $d \leq 2$, the transition to Anderson localized phase is very simple. Any finite amount of disorder W is enough to localize the system, and only if the disorder W is zero, the system can have spatially extended energy eigenstates, which means that the eigenstate thermalization hypothesis for these particular eigenstates is satisfied. In higher dimensions, $d \geq 3$, the transition to Anderson localized phase happens at critical point W_c, that is, the system is in localized phase when $W > W_c$. Hamiltonian eigenstates at the localized phase decays exponentially respect to the distance from localization center. The exponential decay has the form $\psi_\alpha(\boldsymbol{r}) \sim e^{-\frac{|\boldsymbol{r}-\boldsymbol{R_\alpha}|}{\xi}}$, where the ξ is the localization length and $\boldsymbol{R_\alpha}$ is the localization centre. The variables with bold font refer to vectors, thus, the exponentially decaying form of the wave function $\psi_\alpha(\boldsymbol{r})$ is valid in all dimensions. [12, 18]

In dimensions $d \leq 2$, the system is fully localized (i.e. every energy eigenstate decays exponentially) for every disorder strength $W > 0$. However, in higher dimensions the transition is not sharp, and there is a disorder strength interval where some portion of the eigenstates are localized and other are extended. Disorder strengths inside this transition interval are characterized by mobility edge which separates the localized and extended eigenstates by their eigenenergies. Usually the eigenstates below the mobility edge are localized and the ones above are thermal. [12, 18]

The two Hamiltonians (2.4) and (2.5) demonstrate Anderson localization if one neglects the on-site interaction, that is, defining parameters $V = J_z = 0$. Without interactions, it is possible to carry out a basis transformation which changes the Hamiltonian to

following form [18]

$$\hat{H} = \sum_{\alpha} E_{\alpha} \hat{n}_{\alpha}, \tag{2.6}$$

where $\hat{n}_{\alpha}$ is the number operator for single-particle eigenstate $|\alpha\rangle$ and E_{α} is the corresponding eigenenergy. In this simpler representation it makes much sense to write the many-particle eigenstate as a product state of single-particle eigenstates, $|\psi_{\text{eig}}\rangle = \prod_{\alpha} \otimes |\alpha\rangle$, where the tensor product is over every single-particle eigenstate $|\alpha\rangle$.

In Hamiltonians (2.4) and (2.5) (on-site interactions neglected) system is fully localized for any finite amount of disorder W, therefore, these systems do not display a mobility edge. This breakdown of ETH in every energy eigenstate makes it clear that non-equilibrium initial states will not relax to the thermal equilibrium, but in 3D systems, the existence of mobility edge allows the relaxation of some initial states. More specifically, if the initial state has some weight on the eigenstates which violate ETH then the information concerning this part of the initial state will survive indefinitely. In this context non-equilibrium initial state means that the probability density function, which describes the probability for each spin to be populated, is not uniform over all spin sites [12].

In the following section, we discuss how adding on-site interactions into the system will increase its complexity but still allows the existence of a localized phase.

2.2.2 Many-body localization

A localized phase where particles can feel each other through on-site interactions is known as many-body localized (MBL) phase. The problem of localization in the interacting case was already raised by Anderson [1] but it was not thoroughly investigated at that time. There were reasons to be suspicious about the survival of localization in interacting systems, but Ref. [20] suggested the survival of localization for strong enough disorder if the interactions are short-range. In Ref. [21], a non-perturbative approach was applied for quantum dots, and the reference showed that states below particular energy will remain localized.

Major contribution to the investigation of MBL was made in Refs. [2, 3]. Especially the Ref. [2] had a large impact by proving that localized single-particle states do not delocalize if weak and short-range electron-electron interactions are added and temperature remains below non-zero critical temperature T_c, but the localization is immediately annihilated by some weak coupling to external bath. The critical temperature differentiates the insulating and metallic phases and suggests the existence of a many-body mobility edge. The possibility of localized phase with interacting particles in finite temperature

was an interesting discovery because interactions are inevitable in practical situations, and furthermore, MBL is not dependent on fine-tuning of interactions or other parameters. Temperature is not a well-defined quantity if there is no heat bath connected to the system, but if we consider only a small part of the total system, the rest of the system can be considered as the environment (heat bath). In the ergodic phase, the density operator is given by a canonical ensemble which can be used to define the temperature. Of course in the MBL phase, the density operator is not given by the canonical ensemble but the critical temperature is located at the boundary of the ergodic phase and the MBL phase, thus, we can use the ergodic phase to define the critical temperature.

Later, it was argued that MBL would survive even with strong interactions and very high temperature if the disorder is strong enough [4]. The argument was made by using numerically exact diagonalization of model similar to Hamiltonian (2.4). The distinction between thermal and MBL phases is made by using spectral statistics, that is, the nearby energy levels follow the orthogonal random matrix statistics in thermal phase and Poisson statistics in MBL phase. In Ref. [22], numerical exact diagonalization was applied to the spin model in Eq. (2.5) and the numerical results were used to investigate the phase transition between ergodic and MBL phases.

A different numerical approach was used in Ref. [23]. Instead of exact diagonalization, the authors applied a time-dependent density-matrix renormalization group (tDMRG) simulations to investigate the logarithmic growth of entanglement entropy. A similar numerical method is employed in Ref. [24], and it demonstrates the logarithmic growth in an infinite system. The logarithmic growth is an essential characteristic of the MBL phase, and it differentiates the MBL phase from thermal and Anderson localized phases. The propagation of entanglement should not be confused with transport properties of the system (e.g. energy or charge), because these properties are also absent in MBL phase.

Some aspects of the MBL phase transition were investigated in Refs. [25, 26]. Particularly, numerical results concerning the many-body mobility edge were presented, and these results displayed a mobility edge with two boundaries, that is, the eigenstates in the middle of the energy spectrum are thermal and the eigenstates at the bottom/top are localized.

We have noticed that, in 1-D systems, the localization phase transition is dependent on two parameters: Disorder strength W and on-site interaction strength V [in the Hamiltonian (2.4)]. Larger disorder makes the system shift deeper into the localized phase and if interactions become stronger the system usually moves deeper into the delocalized phase. However, the latter claim is not always true since it is possible that for very strong interactions the system moves towards the localized phase, implying

that there can be two critical values for parameter V. The critical value $W_c(V)$ of the disorder strength is dependent on the on-site interactions. System may express localized behaviour below the critical value W_c because of the mobility edge, but $|W| \geq W_c$ defines a region known as fully many-body localized (FMBL) phase, where every many-body eigenstate breaks ETH.

Current decade has provided much intuition for the case of FMBL phase. The intuitive understanding of the FMBL is achieved by introducing the concept of a quasi-local integral of motion (LIOM), also known as l-bit (local bit). These LIOMs implicate a new kind of integrability, which explains the breakdown of ergodicity in the FMBL regime. [27–30]

2.3 Signatures of many-body localization

2.3.1 Emergent integrability

A major difference in eigenstates between ergodic and localized phases is the fact that eigenstates of ergodic phase are, in general, spatially extended over the whole system, while eigenstates of localized phase are exponentially localized as

$$\psi_\alpha(\boldsymbol{r}) \sim e^{-\frac{|\boldsymbol{r}-\boldsymbol{R_\alpha}|}{\xi}}, \tag{2.7}$$

Many-body localized system has multiple interacting excitations and, thus, Eq. (2.7) cannot accurately describe the eigenstates of such system. The exponentially decaying property of localization in many-body localized states should be described with LIOMs (see Eq. (2.12)). However, the exponentially decaying nature of eigenstates in the case of one localized excitation gives us some intuition also for the case of many-body localized system. Local perturbations to Hamiltonian in ergodic phase, in general, have global effect to eigenstates of the system. This makes it hard to predict the changes that ergodic systems go through even under weak perturbations, which coincides with the intuition of ergodic systems behaving in a chaotic way [12]. On the other hand, for systems in the FMBL region, the local perturbation will induce only local effects to any eigenstate of the system. This intuition is the motivation for the LIOM description of MBL Hamiltonian [12, 18, 27–29, 31].

To make the concept of LIOMs more concrete, we use the Heisenberg spin model in Eq. (2.5) as an example. The Hamiltonian is non-diagonal in the base constructed from the product states of eigenvectors of operators $\{\hat{\sigma}_i^z\}$, i.e. $|\{\hat{\sigma}_i^z\}\rangle = |\sigma_1\sigma_2...\sigma_N\rangle\,, \sigma_i = \uparrow, \downarrow$. Regardless of the specific realization of the Hamiltonian (2.5), there exists a unitary

transformation $\hat{U}$, which diagonalizes the Hamiltonian if used in a similarity transformation [13]

$$\hat{H}_{\text{diag}} = \hat{U}^{\dagger}\hat{H}\hat{U}. \tag{2.8}$$

As usual, the columns of matrix $\hat{U}$ describe the eigenstates of the Hamiltonian in the product state basis.

Even if the existence of transformation $\hat{U}$ is not dependent on whether the system is in ergodic or MBL phase, the operators $\hat{U}$ have different qualities in these two phases. Especially, $\hat{U}$ in MBL phase is quasi-local unitary transformation. To be more specific, transformation is quasi-local if it can be sequenced to a form

$$\hat{U} = \prod_{i} ... \hat{U}^{(3)}_{i,i+1,i+2} \hat{U}^{(2)}_{i,i+1}, \tag{2.9}$$

where the operator $\hat{U}^{(n)}_{i,i+1,...,i+n}$ fulfils the inequality

$$\left\| 1 - \hat{U}^{(n)}_{i,i+1,...,i+n} \right\|^2_F < e^{-n/\xi}, \tag{2.10}$$

where the norm must understood as the Frobenius norm [12]. This means that the Hamiltonian (2.5), in MBL phase, can be represented by using a set of LIOMs $\{\hat{\tau}^z_i\}$. The mapping between physical spin operator $\hat{\sigma}^z_i$ and LIOM $\hat{\tau}^z_i$ is the following,

$$\hat{\tau}^z_i = \hat{U}\hat{\sigma}^z_i\hat{U}^{\dagger}. \tag{2.11}$$

Because of the quasi-local nature of $\hat{U}$, the quasi-locality appears also in operators $\{\hat{\tau}^z_i\}$. LIOMs can be expressed as

$$\hat{\tau}^z_i = Z\hat{\sigma}^z_i + \sum_n V^{(n)}_i \hat{O}^{(n)}_i, \tag{2.12}$$

where Z is the finite overlap between $\hat{\tau}^z_i$ and $\hat{\sigma}^z_i$, operator $\hat{O}^{(n)}_i$ contributes only for physical spin sites $i-n, ..., i, ..., i+n$, and $V^{(n)}_i$ is a exponentially decaying function, $V^{(n)}_i \sim e^{-n/\xi}$ [12]. Here ξ is called the localization length, and it indicates the locality of operators $\{\hat{\tau}^z_i\}$. Relation in Eq. (2.12) describes how the support of physical spin operators $\{\hat{\sigma}^z_i\}$ for LIOMs, decays exponentially as distance increases. Graphical demonstration for this relation is shown in Fig. 2 of Ref. [32]. One can also define operators $\hat{\tau}^x_i$ and $\hat{\tau}^y_i$ in the following way [12, 31, 32]:

$$\hat{\tau}^x_i = \hat{U}\hat{\sigma}^x_i\hat{U}^{\dagger}, \quad \hat{\tau}^y_i = \hat{U}\hat{\sigma}^y_i\hat{U}^{\dagger}. \tag{2.13}$$

The operators $\hat{\tau}_i^x$ and $\hat{\tau}_i^y$ act on the quasi-local spins in a similar way as operators $\hat{\sigma}_i^x$ and $\hat{\sigma}_i^x$ operate on the physical spins.

Physical spin operators $\hat{\sigma}_i^z$ have well-known commutation relations

$$[\hat{H}, \hat{\sigma}_i^z] = 0, \;\; [\hat{\sigma}_i^z, \hat{\sigma}_j^z] = 0, \tag{2.14}$$

where one needs to assume that the hopping interaction term, i.e. $J_\perp$ in model (2.5), to be zero. Interestingly, similar commutation relations also hold for operators $\hat{\tau}_i^z$

$$[\hat{H}, \hat{\tau}_i^z] = 0, \;\; [\hat{\tau}_i^z, \hat{\tau}_j^z] = 0, \tag{2.15}$$

which can be established by using Eqs. (2.8) and (2.11). [12, 31, 32]

Operators $\left\{\hat{\tau}_i^a\right\}$, where $a = x, y, z$, and the identity operator could be used as alternative operator basis. The quasi-local character and similarities with physical spin Pauli operators are the reasons why these operators are said to operate on pseudospins, which are "dressed" versions of regular physical spins. As eigenvalues of operators $\left\{\hat{\sigma}_i^a\right\}$ are able to uniquely specify every eigenstate of Hamiltonian if hopping terms between different sites are absent, similarly, LIOMs can uniquely determine the eigenstates of the Hamiltonian when hopping terms are present, and these eigenstates could be intuitively labelled with $\hat{\tau}_i^z$ eigenvalues

$$|\{\hat{\tau}_i^z\}\rangle = |\tau_1 \tau_2 ... \tau_N\rangle \, , \tau_i = \uparrow, \downarrow, \tag{2.16}$$

where $\uparrow$ and $\downarrow$ are labels for the eigenvalues 1 and -1.

Since the Hamiltonian and LIOMs commutate with each other, the Hamiltonian can be described by using only LIOMs. Such pseudospin form of the Hamiltonian can be written as

$$\hat{H}_{\mathrm{MBL}} = \sum_i \tilde{h}_i \hat{\tau}_i^z + \sum_{i,j} J_{ij} \hat{\tau}_i^z \hat{\tau}_j^z + \sum_{n=1}^{\infty} \sum_{i,j,\{k\}} K_{i\{k\}j}^{(n)} \hat{\tau}_i^z \hat{\tau}_{k_1}^z ... \hat{\tau}_{k_n}^z \hat{\tau}_j^z, \tag{2.17}$$

where terms $K_{i\{k\}j}^{(n)}$ are $(n+2)$-LIOM interaction terms, every term is included only once and a possible constant term is shifted to zero [12, 18, 27–32]. Since the MBL Hamiltonian in question was obtained with quasi-local transformation $\hat{U}$, the interactions must also demonstrate, exponentially fading, quasi-local behaviour, as following expressions point out [12, 27, 31]:

$$J_{ij} \propto J_0 e^{-\frac{|i-j|}{\kappa}}, K_{i_1 ... i_{n+2}}^{(n)} \propto J_0 e^{-\frac{\max\left|i_\alpha - i_\beta\right|}{\kappa}}, \tag{2.18}$$

where the length constant κ (dimensionless) is not same as localization length ξ, but it defines the interaction length between LIOMs. The length scale is restricted by the inequality $\kappa^{-1} \geq (\xi^{-1} + \ln 2)/2$, which connects the two length scales together [12]. The MBL presentation of the Hamiltonian in Eq. (2.17) is useful because it reveals some important information about the dynamical behaviour of the system.

One interesting property of Hamiltonian (2.17) follows from the fact that $\hat{H}_{\mathrm{MBL}}$ is constructed by using only LIOMs, therefore, if the system is closed, there is no dissipation in the LIOMs. This situation is closely analogous with the Hamiltonian (2.5) when $J_\perp = 0$ is assumed and only neighbouring physical spins interact with each other. Even though there is no "pseudospin" transport in the system, the interactions between two or more LIOMs allows an increasing entanglement between the LIOM degrees of freedom. This means that initially non-entangled states get entangled under the time evolution dictated by the Hamiltonian (2.17). Furthermore, measuring the rate of entanglement growth in a system can be a differentiating characteristic between Anderson, thermal and MBL phases.

It is important to notice that also Hamiltonians in the ergodic regime can be presented in the form of Eq. (2.17), but the conserved quantities, integrals of motion, have no longer a quasi-local character. This questions the whole usefulness of this representation because quasi-locality of operators $\left\{\hat{\tau}_i^z\right\}$ is the reason why Hamiltonian (2.17) reveals some meaningful insight into dynamical properties of the system.

The rise of conserved local quantities, LIOMs, as the system shifts to MBL phase is often called as emergent integrability of MBL phase. This integrability in MBL systems is robust against weak perturbations, which makes it unique compared to many other common types of integrable systems [12]. Here we will take a closer look on MBL phase from a point of view of entanglement.

2.3.2 Logarithmic growth of entanglement

As mentioned above, there is no transport of spin excitations in model of Eq. (2.5), which is a feature of the localized system, but the absence of transport does not imply the absence of entanglement propagation. In fact, the entanglement growth is one of the defining characteristics of the MBL phase that separates it from the ergodic and Anderson localized phases. In the Anderson localized phase, there is no entanglement propagation since the LIOMs do not have any interactions between each other, e.g. see Eq. (2.6). On the other hand, thermal systems obey a power-law entanglement spreading as a function of time [18, 33]. The most interesting entanglement behaviour is occurring in the MBL phase, in which the propagation of entanglement is logarithmic, separating

it from the other considered phases. This peculiar behaviour is a consequence from an exponentially decreasing effective interactions of MBL Hamiltonian (2.17).

Before tackling a real MBL system in its full complexity, it is helpful to consider a simple system of two spins and examine how entanglement works in this system. For two spins the MBL Hamiltonian reduces to

$$\hat{H}_{\mathrm{MBL}} = J_{12}\hat{\tau}_1^z\hat{\tau}_2^z, \tag{2.19}$$

where the terms with only single LIOM are neglected because those terms are not relevant from the entanglement point of view. We label the eigenstates of each $\hat{\tau}_i^z$ operator as $|\Uparrow_i\rangle$ and $|\Downarrow_i\rangle$. The initial state of the system is chosen to be a non-entangled state, i.e., a product state of two pseudospins:

$$\begin{aligned} |\Psi(t=0)\rangle &= \frac{1}{\sqrt{2}}(|\Uparrow_1\rangle + |\Downarrow_1\rangle) \otimes \frac{1}{\sqrt{2}}(|\Uparrow_2\rangle + |\Downarrow_2\rangle) \\ &= \frac{1}{2}(|\Uparrow\Uparrow\rangle + |\Uparrow\Downarrow\rangle + |\Downarrow\Uparrow\rangle + |\Downarrow\Downarrow\rangle). \end{aligned} \tag{2.20}$$

By operating with unitary time evolution operator $\hat{U} = e^{-i\hat{H}_{\mathrm{MBL}}t}$ ($\hbar$ is neglected) on the initial state, one obtains the time-dependent state

$$|\Psi(t)\rangle = \frac{1}{2}e^{-iJ_{12}t}(|\Uparrow\Uparrow\rangle + |\Downarrow\Downarrow\rangle) + \frac{1}{2}e^{iJ_{12}t}(|\Uparrow\Downarrow\rangle + |\Downarrow\Uparrow\rangle). \tag{2.21}$$

The state in question is pure, therefore, the density operator is defined as

$$\hat{\varrho}(t) = |\Psi(t)\rangle \langle\Psi(t)| . \tag{2.22}$$

The density operator can be expanded in the LIOM eigenbasis as

$$\begin{aligned} \hat{\varrho}(t) = &\frac{1}{4}(|\Uparrow\Uparrow\rangle \langle\Uparrow\Uparrow| + |\Uparrow\Uparrow\rangle \langle\Downarrow\Downarrow| + |\Downarrow\Downarrow\rangle \langle\Uparrow\Uparrow| + |\Downarrow\Downarrow\rangle \langle\Downarrow\Downarrow|) \\ &+ \frac{U}{4}(|\Uparrow\Uparrow\rangle \langle\Uparrow\Downarrow| + |\Uparrow\Uparrow\rangle \langle\Downarrow\Uparrow| + |\Downarrow\Downarrow\rangle \langle\Uparrow\Downarrow| + |\Downarrow\Downarrow\rangle \langle\Downarrow\Uparrow|) \\ &+ \frac{U^*}{4}(|\Uparrow\Downarrow\rangle \langle\Uparrow\Uparrow| + |\Uparrow\Downarrow\rangle \langle\Downarrow\Downarrow| + |\Downarrow\Uparrow\rangle \langle\Uparrow\Uparrow| + |\Downarrow\Uparrow\rangle \langle\Downarrow\Downarrow|) \\ &+ \frac{1}{4}(|\Uparrow\Downarrow\rangle \langle\Uparrow\Downarrow| + |\Uparrow\Downarrow\rangle \langle\Downarrow\Uparrow| + |\Downarrow\Uparrow\rangle \langle\Uparrow\Downarrow| + |\Downarrow\Uparrow\rangle \langle\Downarrow\Uparrow|), \end{aligned} \tag{2.23}$$

where $U = e^{-i2J_{12}t}$. The amount of entanglement between these two pseudospins is measured with entanglement entropy of one pseudospin. In general, entanglement entropy is defined as

$$S = -\operatorname{Tr}(\hat{\varrho}\ln\hat{\varrho}), \tag{2.24}$$

but if one studies the entanglement between two subsystems A and B, the measure of entanglement is

$$S = -\operatorname{Tr}(\hat{\varrho}_{\mathsf{A}} \ln \hat{\varrho}_{\mathsf{A}}) = -\operatorname{Tr}(\hat{\varrho}_{\mathsf{B}} \ln \hat{\varrho}_{\mathsf{B}}), \tag{2.25}$$

where $\hat{\varrho}_{\mathsf{A}} = \operatorname{Tr}_{\mathsf{B}}(\hat{\varrho}_{\mathsf{AB}})$, $\hat{\varrho}_{\mathsf{B}} = \operatorname{Tr}_{\mathsf{A}}(\hat{\varrho}_{\mathsf{AB}})$ and $\hat{\varrho}_{\mathsf{AB}}$ is a density operator of the combined system [34]. The notation $\operatorname{Tr}_{\mathsf{A}}$ stands for a partial trace over the degrees of freedom located in the subsystem A. Here, we measure the entanglement entropy in our two pseudospin system. As equation (2.25) suggests, it does not matter which degree of freedom we trace out, so we might as well choose to use $\hat{\varrho}_1 = \operatorname{Tr}_2(\hat{\varrho})$, for which, we obtain

$$\hat{\varrho}_1(t) = \frac{1}{2}\left|\Uparrow_1\right\rangle\left\langle\Uparrow_1\right| + \frac{\cos(2J_{12}t)}{2}(\left|\Uparrow_1\right\rangle\left\langle\Downarrow_1\right| + \left|\Downarrow_1\right\rangle\left\langle\Uparrow_1\right|) + \frac{1}{2}\left|\Downarrow_1\right\rangle\left\langle\Downarrow_1\right|. \tag{2.26}$$

Clearly, the entanglement entropy is zero at time $t = 0$, and the maximum is achieved when $J_{12}t = \frac{\pi}{4} + n\frac{\pi}{2}$, where n can be any integer. For this two pseudospin system, instead of being monotonic function in time, the entanglement entropy is periodic. As a consequence, it demonstrates quantum revivals.

The periodic behaviour of entanglement is not present in a large MBL system, in which, there is a macroscopic amount of degrees of freedom. For such system, the dynamics is determined by the Hamiltonian

$$\hat{H}_{\mathrm{MBL}} = \sum_{i,j} \hat{J}_{ij}^{\mathrm{eff}} \hat{\tau}_i^z \hat{\tau}_j^z, \tag{2.27}$$

where $\hat{J}_{ij}^{\mathrm{eff}}$ represents the effective interactions between LIOMs i and j and is defined as

$$\hat{J}_{ij}^{\mathrm{eff}} = J_{ij} + \sum_{n=1}^{\infty} \sum_{\{k\}} K_{i\{k\}j}^{(n)} \hat{\tau}_{k_1}^z ... \hat{\tau}_{k_n}^z. \tag{2.28}$$

The effective interactions are known to decay exponentially,

$$\hat{J}_{ij}^{\mathrm{eff}} \sim J_0 e^{-\frac{|i-j|}{\tilde{\xi}}}, \tag{2.29}$$

where $\tilde{\xi}$ (dimensionless) characterizes yet another exponential decay length [12, 18, 27]. One can use the effective interactions $\hat{J}_{ij}^{\mathrm{eff}}$ to determine the time it takes for two pseudospins, separated by distance $x = |i - j|$ (here the distance is an integer quantity, for which the difference between neighbouring states is unity), to get effectively entangled. To be more precise, a pseudospin acquires a phase factor of order one, created by a another spin from a distance x away, that is effectively dictated by [12, 35]

$$\hat{J}_{ij}^{\mathrm{eff}} t \sim 1. \tag{2.30}$$

By combining expressions in Eqs. (2.29) and (2.30) one can easily solve the dependence between the distance entanglement has effectively propagated x_{ent} and time t, which is [12, 27, 35]

$$x_{\text{ent}}(t) \sim \tilde{\xi} \ln (J_0 t). \tag{2.31}$$

Arguments put forward in Refs. [27, 35] show that entropy of entanglement is proportional to $x_{\text{ent}}(t)$, that is

$$S(t) \propto \tilde{\xi} \ln (J_0 t). \tag{2.32}$$

With all this, we can conclude that at time $t(x)$ the entanglement has covered the whole volume between the boundary of the two subsystems and the distance $x(t)$. The entanglement propagates symmetrically in every possible direction. For example, if the one-dimensional system is divided into two subsystems in such way that subsystem A is only one pseudospin (approximately in the middle of the system) and B is its complement. In such case, the subsystem A gets entangled with subsystem B and the propagation of entanglement occurs similarly to both direction. As one can clearly see, the entanglement entropy is increasing as a logarithmic function of time, explaining why it is referred as logarithmic growth of entanglement. The effective interaction length scale $\tilde{\xi}$, which is not same as the length scale κ, is a major component in the determination of the logarithmic propagation speed.

2.3.3 Dephasing dynamics of quasi-local operators

We pointed out earlier that the logarithmic growth of entanglement is a defining characteristic of the MBL phase, separating it from the other relevant phases. However, the measurement of entanglement is hard to realize in experiments, and therefore, there is a need to find alternative defining characteristics, which are more applicable for experiments [12].

More feasible method, from the experimental point of view, is to measure a quasi-local observable, and study the dephasing dynamics of the operator corresponding to that observable. The quasi-local operators (e.g. pseudospin operators $\hat{\tau}_i^{x,y}$) obey dephasing dynamics which are specific for the MBL phase. These quasi-local observables approach an equilibrium value, after a long time. This convergence to the equilibrium follows a power-law, which is related to a logarithmic growth of entanglement in Eq. (2.31), and therefore also to the exponential decay of effective interactions, see Eq. (2.29). In Refs. [12, 36], the power-law decay is approximated as

$$\left| \langle \hat{\tau}_i^{x,y}(t) \rangle \right| \sim \frac{1}{\sqrt{\mathcal{D}(t)}} \approx \frac{1}{(J_0 t)^a}, \tag{2.33}$$

where $\mathcal{D}(t) \approx 2^{2x(t)}$ is the number of Hilbert space dimensions that are entangled with the pseudospin $\hat{\tau}_i$, at time t, and $a = \tilde{\xi} s_0$. One can see that the exponent of the power-law depends on the effective interaction length $\tilde{\xi}$ and diagonal entropy of the initial state per spin s_0 [35]. Eq. (2.33) shows that the expectation values of the pseudospin operators approach to zero as the whole system becomes entangled (assuming the system has a macroscopic amount of degrees of freedom). This can be rationalized by using a density matrix approach: Entanglement causes the individual pseudospin to lose its quantum coherence, i.e. the off diagonal elements of the density matrix vanish [37], as Eq. (2.26) demonstrates. In the eigenbasis of the MBL Hamiltonian (2.17), the diagonal matrix elements of $\hat{\tau}_i^{x,y}$ are equal to zero. It is easy to see that the expectation value

$$\langle \hat{\tau}_i^{x,y}(t) \rangle = \mathrm{Tr}\left[\hat{\tau}_i^{x,y}(t)\varrho_i(t)\right] = \langle \Uparrow_i | \hat{\tau}_i^{x,y}(t)\varrho_i(t) | \Uparrow_i \rangle + \langle \Downarrow_i | \hat{\tau}_i^{x,y}(t)\varrho_i(t) | \Downarrow_i \rangle \tag{2.34}$$

converges to zero at the long-time limit. However, these quasi-local observables preserve some information of the initial state even in the equilibrium [12]. Since the approach to the equilibrium is due to pure dephasing, one can use the spin-echo methods to retain some of the lost information about the initial state [12, 38, 39].

2.3.4 Area-law entanglement in MBL eigenstates

One defining characteristic of localization (both Anderson and MBL) is area-law entanglement of energy eigenstates. This means that entanglement between a subsystem A and the rest of the system B, increases proportionally to the border area which separates the two subsystems

$$S \propto \mathrm{Vol}(\partial \mathsf{A}), \tag{2.35}$$

where S is the entanglement entropy and $\partial\mathsf{A}$ is the border area of the subsystem A [12, 28]. In this case, $\mathsf{B} = \mathcal{H}/\mathsf{A}$, where $\mathcal{H}$ is the Hilbert space of the complete system. On the other hand, a system in an ergodic phase has eigenstates for which the entanglement increases with the volume of the subsystem A,

$$S \propto \mathrm{Vol}(\mathsf{A}). \tag{2.36}$$

This area-law can be understood by using the same intuition as we used with the MBL Hamiltonian, that is, quasi-local perturbations to a system occupying the localized phase induce only local changes to the eigenstates of the system. This intuition is utilised in the argument presented in Ref. [28]. Briefly, the argument goes as follows: The Hamiltonian

[e.g. model of Eq. (2.5)] is divided in three terms

$$\hat{H} = \hat{H}_{\mathsf{A}} + \hat{H}_{\mathsf{B}} + \hat{V}_{\mathsf{AB}}, \tag{2.37}$$

where $\hat{H}_{\mathsf{A}}$ and $\hat{H}_{\mathsf{B}}$ consists only terms which operate on degrees of freedom that belong to set A, B, and terms that have both belong to $\hat{V}_{\mathsf{AB}}$. If $\hat{V}_{\mathsf{AB}}$ is zero, the energy eigenstates of $\hat{H}$ are product states of $\hat{H}_{\mathsf{A}}$ and $\hat{H}_{\mathsf{B}}$ eigenstates,

$$|\alpha\beta\rangle = |\alpha\rangle_{\mathsf{A}} \otimes |\beta\rangle_{\mathsf{B}}\,, \tag{2.38}$$

therefore, the entanglement between the regions A and B is zero. If a finite interaction term $\hat{V}_{\mathsf{AB}}$ is introduced, regions A and B become entangled. At this point we can exploit the intuition stated above (local perturbation makes only local changes to eigenstates). To be more precise, $\hat{V}_{\mathsf{AB}}$ has a significant effect to spins which are located less than distance ξ away from the boundary between sets A and B. The distance ξ is the same localization length, that we have encountered before.

It is quite reasonable to conclude that spins less than ξ away from boundary become entangled, which means that the entanglement growth is proportional to the area of the boundary. Furthermore, this behaviour was confirmed by the numerical calculations made in Refs. [28, 40].

Chapter 3

Reflection spectroscopy and Fermi's golden rule

So far, our treatment of MBL has been for completely isolated systems, which is also the case for the most of the literature written on the subject. Isolated systems demonstrate the characteristics of MBL much clearer compared to a system with non-zero coupling to an environment. The coupling with the environment reduces the sharpness of the distinctions between the thermal and the MBL phases, and it can easily decimate the whole localization. Unfortunately, the convenient isolated models do not represent the reality accurately, since any system always has a finite coupling to the environment. This more realistic approach to MBL systems was taken in Refs. [41, 42].

The progress in the experimental side of MBL studies might be much easier to fit into the theoretical picture of MBL if the effects of imperfect isolation are known. This is the main premise behind Refs. [41, 42], and it is also the main motivation for this thesis. The approaches used to study the MBL system are very similar in both cases. The method used in this thesis is a spectroscopic method, in which the system is probed by a local perturbation, and the amplitude of the reflected (or absorbed) part of the spectrum, for each frequency, is calculated. This information allows us to construct the energy spectrum of the possible transitions between energy eigenstates, induced by a certain probe. The transition spectrum can reveal important information about the dynamical phase of the system. Furthermore, it can differentiate the localized and the ergodic phases from each other.

This chapter focuses on the relevant theory that is needed to obtain and analyze the transition spectrum. We review the theory presented in Ref. [41], talk about the spectral functions calculated in Ref. [42], and also review the theory of Fermi's golden rule which is relevant for the numerical calculations, presented later.

3.1 Spectral diagnostics of many-body localization

In chapter 2, we introduced many different characteristics of the MBL phase, some distinct to a localized phase in general and others specific for the MBL. Here, we discuss what a transition spectrum can tell us about the dynamical phase of the system.

In Ref. [41], the basic premise is a 1-dimensional chain of interacting spin-$\frac{1}{2}$ particles [for example, the model of Eq. (2.5)]. If the disorder in the on-site potential of each physical spin is large enough, the system can be described with quasi-local integrals of motion (LIOMs), as is done in the MBL Hamiltonian (2.17). The separation with the Anderson localization comes from the non-zero effective interactions in Eq. (2.28). In addition to the MBL system, a bath consisting of interacting bosons is assumed. A bath with interacting particles represents real-world situations well, and it can be described with the following Hamiltonian [41]

$$\hat{H}_{\text{bath}} = J \sum_{\langle ij \rangle} \hat{b}_i^\dagger \hat{b}_j + \Lambda \sum_{\langle ijk \rangle} (\hat{b}_i^\dagger \hat{b}_j^\dagger \hat{b}_k + \hat{b}_i \hat{b}_j \hat{b}_k^\dagger), \tag{3.1}$$

where the first sum term is the harmonic part, and the second sum term is the anharmonic part, induced by the interactions. Parameters J and Λ denote the strength of the harmonic and anharmonic parts, respectively. The operators $\hat{b}_i$ and $\hat{b}_i^\dagger$ denote the annihilation and creation operators, respectively. It is also assumed that Eq. (3.1) describes a "broad bandwidth bath", that is, the energy scale of the bath is much larger compared to characteristic energy scales of the system. This assures that bath can provide the needed energy for any local process occurring in the system. Furthermore, the bath has a large energy diffusivity, leading to effectively Markovian behaviour, that is, the future state of the bath does not depend on any state in the past, it is affected only by the current state. To make sure that the bath is well-behaving, yet another assumption is made: Each site can be occupied, at most, by some finite number of excitations (e.g. two in Ref. [41]).

If we want that the bath has any relevant effect on our system, we need to define interactions between the system and bath. To make the interactions simple, the following interaction Hamiltonian is chosen,

$$\hat{H}_{\text{int}} = g \sum_{\langle i \rangle} \hat{\tau}_i^x (\hat{b}_i^\dagger + \hat{b}_i), \tag{3.2}$$

where the LIOMs are coupled with the local degrees of freedom of the bath. Parameter g represents the coupling strength between the degrees of freedom of the system and the bath. Generally, the rule for system-bath interactions is, that the interaction must

be local in a space of physical spins. This implies that also coupling to the LIOMs is allowed [41].

It is argued that a coupling to a bath with a macroscopic amount of degrees of freedom, ultimately thermalizes the system [41]. On the other hand, the situation in which the system and the bath are finite-sized, the final result is not that clear. In some cases the system still thermalizes, but respectively, it is also possible that a localization of the system might spread into the bath, making the bath effectively localized. This kind of back action, from the system to the bath, was studied in Ref. [43].

3.1.1 Interpretation of the spectral function

In this subsection, we explain the relevant spectral features of the transition spectrum at the limit of perfect isolation. Here it is assumed that the probe operator is the pseudospin-flip operator $\hat{\tau}_i^x$, but in general, there is no qualitative difference in the transition spectrum characteristics, as long as the probe operator is local [18]. The spectral function describing the probe, in a system including the bath, is defined as

$$A_i(\omega) \equiv \mathrm{Im} \int_0^\infty dt\ e^{i\omega t}\, \mathrm{Tr}\Big[\hat{\varrho}\hat{\tau}_i^- e^{-i\hat{H}t}\hat{\tau}_i^+ e^{i\hat{H}t}\Big] + \mathrm{Im} \int_0^\infty dt\ e^{i\omega t}\, \mathrm{Tr}\Big[\hat{\varrho}\hat{\tau}_i^+ e^{-i\hat{H}t}\hat{\tau}_i^- e^{i\hat{H}t}\Big], \tag{3.3}$$

where we have used the well-known Pauli-matrix relation $\hat{\tau}_i^x = \hat{\tau}_i^+ + \hat{\tau}_i^-$. Here $\hat{\varrho}$ denotes the density operator, and the Hamiltonian is defined as [41]

$$\hat{H} = \hat{H}_0 + \hat{H}_{\mathrm{bath}} + \hat{H}_{\mathrm{int}}, \tag{3.4}$$

where $\hat{H}_0$ is denotes the MBL Hamiltonian in Eq. (2.17).

It is important to notice that the operators which constitute the spectral function $A_i(\omega)$, are expressed in the Heisenberg picture [13]. Here, we observe more clearly that the trace operations in Eq. (3.3) are just autocorrelation functions over time

$$\langle \hat{\tau}_i^-(0)\hat{\tau}_i^+(t)\rangle = \mathrm{Tr}\Big[\varrho\hat{\tau}_i^- e^{-i\hat{H}t}\hat{\tau}_i^+ e^{i\hat{H}t}\Big], \quad \langle \hat{\tau}_i^+(0)\hat{\tau}_i^-(t)\rangle = \mathrm{Tr}\Big[\varrho\hat{\tau}_i^+ e^{-i\hat{H}t}\hat{\tau}_i^- e^{i\hat{H}t}\Big]. \tag{3.5}$$

Furthermore, the integrals over time are Fourier transformations of the autocorrelation functions in Eqs. (3.5). This Fourier transformed quantity is known as the response function in the frequency space, which means that the autocorrelation functions must be interpreted as linear response functions in the temporal space [10, 37]. In a more general form, the linear response theory states that

$$\chi(\omega) = \int_{-\infty}^{\infty} dt\ e^{i\omega t}\chi(t), \tag{3.6}$$

where χ is the response function which is transformed into the frequency space by using the Fourier transform. In general, the response function is a complex function

$$\chi(\omega) = \chi'(\omega) + i\chi''(\omega), \tag{3.7}$$

where $\chi'(\omega)$ is known as the reactive part of response function, and $\chi''(\omega)$ is known as the dissipative (or absorptive) part. Causality prevents us from affecting the past and, thus, the response function must be limited by the condition, $\chi(t < 0) = 0$, which means that we can reduce the integral in Eq. (3.6) to the form

$$\chi(\omega) = \int_0^\infty dt\ e^{i\omega t}\chi(t). \tag{3.8}$$

By using this insight of linear response theory to our system, we can understand the spectral function in equation (3.3) more thoroughly. The response function in the system is

$$\chi(t) = \langle \hat{\tau}_i^-(0)\hat{\tau}_i^+(t)\rangle + \langle \hat{\tau}_i^+(0)\hat{\tau}_i^-(t)\rangle\,, \tag{3.9}$$

and the spectral function is equal to the dissipative part of the response function, $A(\omega) = \mathrm{Im}[\chi(\omega)] = \chi''(\omega)$. Because the task is to study the transitions between the eigenstates of the system, we are only interested in the dissipative part of response function, since it is the part which defines the absorption spectrum. [44]

3.1.2 Spectral function at zero-coupling limit and for temperature T

The simplest case for the interpretation of the absorption spectrum is obtained if the coupling to environment g is zero and the system temperature T is zero. This means, that the system occupies solely the ground state. The pseudospin flip operators, $\hat{\tau}_i^x$, used to probe the system, induce transitions from one energy eigenstate (ground state) to some other energy eigenstate, by changing the orientation of i^{th} LIOM to the opposite direction. Furthermore, the isolation from the environment means that the transitions between eigenstates occur only if the angular frequency ω of the probe is exactly equal to the transition angular frequency between initial and final eigenstates, $\Delta\omega = (E_f - E_i)/\hbar$. All this means, that the spectral function is proportional to just one delta function

$$A_i(\omega) \propto \delta(\Delta\omega - \omega). \tag{3.10}$$

More generally, we could consider the system in a non-zero temperature. In this case, the initial state is no longer equal to the ground state, but is described by the canonical

ensemble [8]

$$\hat{\varrho}(T) = \frac{1}{Z(T)} e^{-\beta(T)\hat{H}}, \tag{3.11}$$

where $\beta(T) = \frac{1}{k_B T}$ (k_B is the Boltzmann constant) and

$$Z(T) = \sum_i e^{-\beta(T)E_i} \tag{3.12}$$

is the partition function. Here, it is possible that the spectral function has as many δ-functions as there are possible initial states. The canonical ensemble implies that the probability for the system to be in an eigenstate decreases as a function of energy and, therefore, the transitions from high-energy initial states have lower spectral function amplitude compared transitions of which initial state energy is low. This means, that the transitions from the low-energy eigenstates to high-energy ones are more probable compared to transitions from the high-energy eigenstates to the low-energy eigenstates. This is demonstrated by the asymmetric behaviour of the spectral function and, moreover, the condition $A_i(\omega) \geq A_i(-\omega), \forall\omega$ is satisfied.

There is a special case for this setup. If we assume a system at the limit of infinite temperature, the density operator will reduce to

$$\hat{\varrho}(T = \infty) = \lim_{T\to\infty} \frac{1}{Z(T)} e^{-\beta(T)\hat{H}} = \frac{1}{N}, \tag{3.13}$$

where N denotes the number of energy eigenstates. This means that every eigenstate in the ensemble of Eq. (3.13) has equal probabilities and, therefore, the spectral function obeys the condition $A_i(\omega) = A_i(-\omega)$, that is, the spectral function is symmetric.

3.1.3 How interactions affect the spectral function?

Since our motivation to study the spectral functions comes from the need to differentiate the ergodic phase from the MBL phase, and the interaction strength between the excitations being one of the crucial parameters defining the phase transition, we need to investigate how the spectral function changes between the regions with and without interactions.

As we discussed above, the Hamiltonian written by using the integrals of motion, $\{\hat{\tau}_i^z\}$, has the form given in in Eq. (2.17). We noticed that simple nearest-neighbour interactions in the physical spin picture in Eq. (2.5) induces such interactions in integral of motion picture that each pseudospin interacts with every other pseudospin. These effective interactions are presented in Eq. (2.28). The important point, in the context of

MBL, was the exponential decay of pseudospin interactions as a function of the distance, which is shown in Eq. (2.29).

In general, the interactions increase the complexity of the spectral function. Without interactions, the infinite temperature setup we discussed earlier (see Eq. (3.13)), has only two δ-peaks, which are symmetric respect to the angular frequency variable ω [42]. Compared to the situation in which the interactions are present, the number of spectral function peaks has dropped from the total number of energy eigenstates to only two. The reason for this reduction of complexity becomes clear if we calculate the energy level separation between the initial and final states of the transition which is induced by a probe proportional to the operator $\hat{\tau}_j^x$. The energy difference can be calculated as follows:

$$\Delta E = \langle u_f | \hat{H}_{\mathrm{MBL}} | u_f \rangle - \langle u_i | \hat{H}_{\mathrm{MBL}} | u_i \rangle = 2\tilde{h}_l + \sum_{j,k} \langle u_f | J_{jk}^{\mathrm{eff}} \hat{\tau}_j^z \hat{\tau}_k^z | u_f \rangle - \sum_{j,k} \langle u_i | J_{jk}^{\mathrm{eff}} \hat{\tau}_j^z \hat{\tau}_k^z | u_i \rangle \,, \tag{3.14}$$

where we have assumed $|u_f\rangle = |... \Uparrow_l ...\rangle$ and $|u_i\rangle = |... \Downarrow_l ...\rangle$ to be some energy eigenstate which differ from each other by only one spin flip at site j. Also we have assumed that the eigenvalues corresponding to operator $\hat{\tau}_j^z$ are 1 and -1 for all sites j. If the interactions are zero, we obtain that the transition energy from $|u_f\rangle$ to $|u_i\rangle$ is same for all possible eigenstates, $\Delta E = 2\tilde{h}_l$. On the other hand, in the presence of interactions, we obtain different transition energies for every possible choice of eigenkets $|u_f\rangle$ and $|u_i\rangle$. This division of transition peaks in the spectrum is the characteristic difference between the Anderson localization and the MBL in the context of spectral function approach (see figures in the supplemental materials of Ref. [42]).

The answer to the question we posed above about the role of interactions in the spectral functions is the following: Interactions divide each transition peak to smaller peaks, where the number of peaks is given by the number of energy eigenstates. For systems that approach the thermodynamic limit, the number of transition peaks is be infinite. The interesting question is, whether the spectral function with an infinite amount of δ-peaks is continuous or discrete.

3.1.4 Weak and strong regimes of MBL

It was stated above that the interacting spin-chain Hamiltonian (2.5), written by using only the integrals of motion of Eq. (2.17), has effective interactions given by Eq. (2.28). One of the central characteristics of the MBL phase is that effective interactions decay exponentially with the distance between pseudospins, as seen in Eq. (2.29).

This tells us something relevant about the δ-function distribution of the spectral function. In the MBL phase, the contribution made by distant pseudospins is exponentially small. In other words, the energy difference between δ-functions decays exponentially fast as a function of the distance. This creates a "spectral tree" structure in which the "tree" divides into new branches, as we take account the interacting pseudospins at further distance, but the size of the branch becomes undetectable if it is created by an interaction with a distant pseudospin [41] (a visualization for such "spectral tree" structure is given in Fig. 1 of Ref. [41]). The branching ratio for our system is four, since increasing distance x of the accounted pseudospins, by one, will include two new pseudospins, which can have four different orientations altogether.

Here, we want to know how the average gap between δ-functions scales, as a function of distance x between pseudospins if effective interactions decay exponentially and the branching ratio is four. If the distance is $x = 1$, the average gap is $J_0/4$. This allows us to solve the characteristic length scale $\tilde{\xi}$:

$$J_0 e^{-1/\tilde{\xi}} \sim J_0/4 \;\Rightarrow\; \tilde{\xi} \sim \frac{1}{\ln 4}. \tag{3.15}$$

Therefore, the average gap scales as $\sim J_0 e^{-x \ln 4}$ [41]. Furthermore, the value $1/\ln 4$ for the characteristic length separates two qualitatively different regimes of behaviour.

If we have a spin system in the MBL phase with the interaction decay length $\tilde{\xi} < 1/\ln 4$, the typical energy gaps between δ-functions $\sim J_0 e^{-x/\tilde{\xi}}$ become small compared to the average gap as x increases. Because of this, different branches of the spectral tree cross each other rarely, meaning that the spectral structure resembles a Cantor set, as $x \to \infty$. Similarity with the Cantor set comes from the fact that the spectral function has infinitely many discrete spectral lines, separated by infinite number of spectral gaps [41]. This kind of behaviour occurs if the range of the effective interactions is short, which implies that the system is deeply localized. Thus this regime known as strong MBL.

On the other hand, if a typical energy scale for branching is larger than the average energy scale, that is $\tilde{\xi} > 1/\ln 4$, then the different branches of the spectral tree have plenty of crossings between each other. This means that for $x \to \infty$, there is an infinite number of δ-functions and almost every spectral gap is densely filled. This kind of structure is continuous and it is called weak MBL. [41]

Naturally, if we increase the effective interaction length to the limit $\tilde{\xi} \to \infty$, the system goes through a delocalization transition from the MBL phase to the ergodic phase. Thus, also the spectral function of the system in the ergodic phase is also continuous and, therefore, continuity is not a differentiating factor between weak MBL and ergodic phases. Fortunately, the MBL phase has a universal spectral characteristic, which can

be used to separate both weak MBL and strong MBL from the ergodic phase. The characteristic is known as the soft gap, which is a gap in the spectral function at $\omega \to 0$. This is a direct manifestation of vanishing dc transport properties of the localized systems. [41]

3.1.5 Strong-weak MBL transition in finite temperature

So far we have analyzed the spectral function in an infinite temperature. Although the infinite temperature is not very realistic, the eigenstates with equal probabilities make it easier to obtain the results and analyse them from a spectral perspective. However, we could consider a system with finite temperature and try to discover the critical value for the effective interaction length $\tilde{\xi}$ for which the transition between weak and strong MBL takes place.

The important thing which changes for finite temperature is the equal probabilities of energy eigenstates. Thus, the transitions are effectively occurring in some subset of all eigenstates. Lower temperature means a smaller subset. A useful measure for the size of this subset is the entropy of entanglement per spin, which is defined as

$$s(T) = \frac{S(T)}{\Lambda} = -\frac{1}{\Lambda}\,\mathrm{Tr}(\hat{\varrho}\ln\hat{\varrho}), \tag{3.16}$$

where S is the total entanglement entropy and Λ is the total number of spins in the system [41]. We use the fact that the system is in the maximum entropy state for $T \to \infty$, and calculate the maximum value for s, where we also use the relation $N = 2^{\Lambda}$ between number of spins Λ and the number of degrees of freedom N. This gives us the maximum value

$$s(\infty) = -\frac{1}{\log_2 N}\sum_{j=1}^{N}\frac{1}{N}\ln\left(\frac{1}{N}\right) = -\frac{\ln 2}{\ln N}\ln\left(\frac{1}{N}\right) = \ln 2, \tag{3.17}$$

which is not affected by the size of the system. Clearly for a finite temperature, it must be true that $0 < s(T) < \ln 2$, where the lower limit corresponds to $s(T = 0) = 0$.

We already know that the branching ratio for an infinite temperature is four, and the number of δ-functions, caused by the effective interactions, increases as a function of the interaction distance $2^{2x_{\mathrm{int}}}$, where x_{int} is the interaction distance (If interactions are only reaching nearest-neighbours $x_{\mathrm{int}} = 1$ and the branching ratio is four). Naturally, if the temperature is finite, the branching ratio is less than four, and we obtain an approximate form for the temperature dependent branching ratio, by using the entanglement entropy per spin. This results in to a following order of magnitude for the branching ratio, $\sim e^{2x_{\mathrm{int}}\,s(T)}$, which clearly holds for the limiting values $T \to 0$ and $T \to \infty$. If we equate

the branching ratio with the typical splitting $J_0 e^{-n/\tilde{\xi}}$ similarly as we did in Eq. (3.15), we obtain the following relation:

$$J_0 e^{-n/\tilde{\xi}(T)} \sim J_0 e^{-2ns(T)} \;\Rightarrow\; \tilde{\xi}(T) = \frac{1}{2s(T)}. \tag{3.18}$$

Therefore in general, the transition between the weak and strong MBL occurs at $\tilde{\xi} = \frac{1}{2s(T)}$, at thermodynamic limit $\Lambda \to \infty$. [41]

3.1.6 The universal characteristic of localization

So far, our discussion has been limited to a situation where the system is perturbed with only one local probe, targeted to just one pseudospin. This approach leads to a spectral distinction between the weak and strong MBL at the thermodynamic limit. Let us consider two pseudospin flip probes, both of which are similar to the single-pseudospin-flip probe üsed earlier for the spectral function in Eq. (3.3). Only difference between these probes is, that they affect different sites and do not excite the same pseudospin. In the strong MBL phase, both of these probes generate an absorption spectrum with an infinite number of discrete spectral lines, separated by infinitely many spectral gaps. In general, the spectral lines and gaps caused by the probes do not coincide. This means that in the case of multiple local probes the discrete spectral structure vanishes and turns into a continuous spectrum, effectively demolishing the distinction between the strong and weak MBL [41]. The procedure in which the spectra from different probes (targeted to different sites) are summed into one spectrum, is known as spatial averaging.

In the process of spatial averaging, most of the spectral gaps vanish, but the zero frequency gap known as the soft gap is not affected. As stated above, the soft gap is known as a universal characteristic of localization and, thus, it is present in both Anderson localized and MBL phases. It survives from the spatial averaging since it always appears at $\omega \to 0$.

Soft gap can be explained with a phenomenon called energy level repulsion. It occurs in systems, whose unperturbed energy eigenstates are connected by a non-commuting perturbation term (i.e. off-diagonal in the eigenbasis of the unperturbed system). In our spin system in Eq. (2.5), the non-commuting term is the one describing the hopping of excitations. The strength of the repulsion depends on the strength of the perturbation and, naturally, repulsion is stronger if the energy levels are closer to each other. Furthermore, the energy level repulsion can occur only if the corresponding eigenstates can "feel" each other. In a situation where two eigenstates are directly connected with a hopping term, it is clear that energy level repulsion can occur. To make this more concrete, we consider a simple two-state system with unperturbed eigenenergies E_1 and

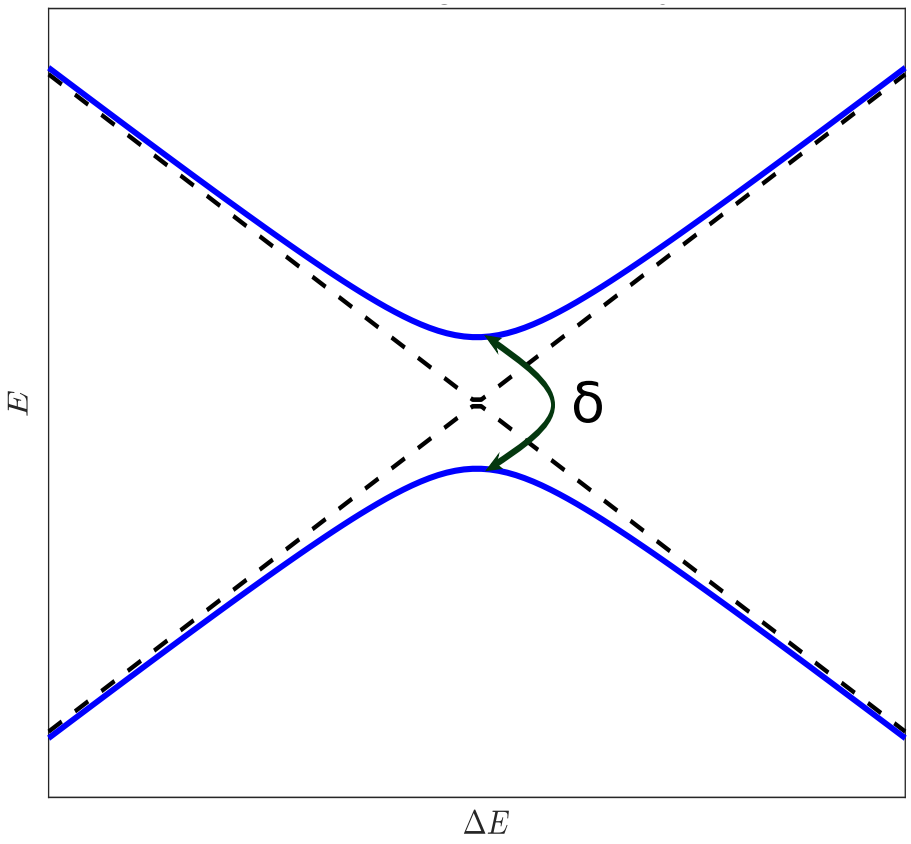

FIGURE 3.1: Behaviour of the eigenenergies of a two-state system. The solid blue line describes the case where level repulsion appears. The size of this avoided crossing is determined by the strength of the coupling δ. The case were coupling strength $\delta = 0$, that is, there is no level repulsion is described by dashed line (black).

E_2. We introduce a perturbation that is symmetric and non-commuting with the unperturbed Hamiltonian. The perturbed Hamiltonian can be written in the unperturbed eigenbasis in a matrix form as

$$\hat{H} = \hat{H}_0 + \hat{V} = \begin{bmatrix} E_1 & 0 \\ 0 & E_2 \end{bmatrix} + \begin{bmatrix} \delta_1 & \delta \\ \delta & \delta_2 \end{bmatrix},$$

where $\hat{H}_0$ is the unperturbed Hamiltonian and $\hat{V}$ is the perturbation. Perturbed eigenvalues are obtained from the equation

$$E_\pm = \frac{1}{2}(E_1 + E_2 + \delta_1 + \delta_2) \pm \frac{1}{2}\sqrt{(E_1 - E_2 + \delta_1 - \delta_2)^2 + 4\delta^2}, \tag{3.19}$$

where the second term is responsible for the level repulsion. We can see that the level repulsion vanishes if $\delta \to 0$ or $E_1 - E_2 \to \infty$ [13]. However, if eigenstates are not directly

connected, but instead it requires multiple hopping terms to reach the other eigenstate, the possibility of level repulsion is not that clear. This case is studied more thoroughly in Refs. [45, 46].

To expand on how the level repulsion affects the existence of the soft gap, we recall the spectral statistics of the MBL and thermal phases. Spectral statistics describes the probability distribution of the distance ratio r_α between adjacent energy levels, defined as [4, 6]

$$r_\alpha = \frac{\min\{s_\alpha, s_{\alpha-1}\}}{\max\{s_\alpha, s_{\alpha-1}\}}, \qquad s_\alpha = E_{\alpha+1} - E_\alpha. \tag{3.20}$$

The probability distribution in the thermal phase takes a form of a Gaussian orthogonal ensemble and the MBL phase follows the Poisson distribution at the thermodynamic limit [4, 6]. The crucial difference between the two distributions is the behaviour at $r_\alpha \to 0$, where Poisson distribution approaches a finite value and the Gaussian orthogonal ensemble goes to zero. In the MBL phase, there can be many degenerate energy levels which do not experience any level repulsion. This occurs if the distance between the corresponding eigenstates is long enough so that the eigenstates do not "feel" each other. On the other hand, in the thermal phase, the probability goes to zero for small r_α. This is because, in general, there is a level repulsion between most of the energy levels and, therefore, the difference between $\min\{s_\alpha\}$ and $\max\{s_\alpha\}$ is much smaller [41].

One can argue that the level repulsion has to do with the symmetries of the system [47]. In the thermal phase, there are no local integrals of motion, which means that the eigenstates are global. These global eigenstates have a significant spatial overlap with each other, which explains why the energy levels are "feeling" changes in the other energy levels. In the MBL region, the system has integrals of motion that are local, which means that any chosen eigenstate has only a vanishing spatial overlap with other eigenstates, in general. The local integrals of motion are the reason why the system becomes integrable in the MBL phase. In fact, the suppression of level repulsion is a general property of integrable systems, contrasting the chaotic systems in which the level repulsion is one of the main characteristics [47].

At first sight, the fact that there can be degenerate energy levels in the MBL phase might seem like a contradiction with the soft gap, which is a universal property of localized systems. However, the contradiction is solved if we examine the transition probabilities. These probabilities are proportional to the off-diagonal elements of perturbing operator, i.e. the pseudospin flip $\hat{\tau}_i^x$ in our example [48], i.e.

$$\mathcal{P}_{if} \propto \left| \langle u_i | \hat{\tau}_i^x | u_f \rangle \right|^2, \tag{3.21}$$

where $|u_i\rangle$ and $|u_f\rangle$ refer to initial and final eigenstates. Again, we employ the fact that the MBL eigenstates have only exponentially vanishing overlap with the distant eigenstates, which implies that for every local operator the transition probability also vanishes exponentially. Here, the reason for the existence of the soft gap is clear: Two eigenstates separated by a short distance exhibit level repulsion and for distant degenerate eigenstates the transition rate is very small. By distant and degenerate eigenstates, we mean eigenstates which have approximately the same energy and vanishingly small overlap, that is, the inner product between these eigenstates is vanishingly small.

We solved the contradiction concerning the MBL phase, but one might also perceive the susceptibility of the thermal phase to level repulsion to be a contradiction to the soft gap. One might think that if all energy levels are repelling each other, then there must be a soft gap. In fact, it is possible for a thermal phase to have a spectral gap as $\omega \to 0$, if the system size does not approach the thermodynamic limit. However, this gap differs from the soft gap since the behaviour at low frequencies is described with a different exponent value. The soft gap has the form $\sim \omega^\mu$, where $1 < \mu < 2$, but in the thermal side of the transition the exponent has values between $0 \leq \mu < 1$ [45]. As we approach the thermodynamic limit, the gap completely vanishes. The vanishing gap is explained with the level repulsion affecting only at the scale of the many-body level spacing, which decreases exponentially with the size of the system. Therefore, the soft gap vanishes in the thermodynamic limit [41].

3.1.7 The role of dissipation

So far we have studied only systems with zero coupling with the environment. If the system is independent from the environment there cannot be dissipation and, in the presence of an external probe, the absorption spectrum consists only of perfect δ-functions. In the case of a finite coupling g, the δ-functions are deformed into Lorentzian functions which define the new transition rates

$$\mathcal{P}_{if} \propto \frac{1}{2\pi} \frac{\Gamma(g)}{(\Delta E - \omega)^2 - \frac{1}{4}\Gamma^2(g)}, \tag{3.22}$$

where $\Gamma(g)$ is the width of the Lorentzian, and it is a function of the environment coupling strength g. The spectral analysis, that was introduced above, focused on the relations between spectral lines and gaps. Therefore, the new Lorentzian spectral lines might smear out some of the spectral structure that can be observed in the case of no dissipation. Specifically, it is easy to see that the structure of infinite gaps, defining the strong MBL, is not recognizable if the spectral lines have finite widths, although, weak and strong MBL still have qualitative differences as long as $\Gamma(g) \ll J_0$, where J_0 is the

amplitude of the effective interactions [41]. If the line-broadening is not too large, there are many gaps, which are only weakly filled. Even the soft gap is no longer strictly a gap, since it is also weakly filled, but the remains of the soft gap are visible if $\tilde{\Delta} > \Gamma(g)$, where $\tilde{\Delta}$ is the size of the soft gap. It is important to note that a thermal bath (bath with thermal eigenstates, which refers to eigenstates that obey the eigenstate thermalization hypothesis) with a macroscopic size and a finite coupling strength g results in effectively thermal eigenstates of the whole system (bath is included) [41].

3.1.8 What about probes coupled to physical spins?

Until this point, we have only considered probes proportional to pseudospin flip operator $\hat{\tau}_i^x$. Theoretically, such operators are easy to handle, since they affect only one pseudospin, but practically it is much easier to produce probes which affect only the physical spin, e.g. a physical spin-flip operator $\hat{\sigma}_i^x$. Fortunately, the results obtained for physical spin probes have similar qualitative properties as the probes coupled to pseudospins. As discussed above, physical spins and pseudospins have a considerable amount of overlap, at least in the case of a small localization length ξ and, thus, we anticipate similar spectral functions for both cases. The soft gap is clearly observable in the case of physical spin probes, but also one can expect a distinction for the weak and strong MBL for small enough ξ.

3.2 Fermi's golden rule

The spectrum describing transitions between the energy eigenstates of the system is the main interest of this thesis. Above, we have considered this spectrum from the point of view of the absorption spectrum in Eq. (3.3). However, it turns out that there is an alternative and equivalent way to approach this problem. This alternative is known as Fermi's golden rule. In the following, we present a short derivation of Fermi's golden rule and show that it is equal with the absorption spectrum in Eq. (3.3) approach.

3.2.1 Derivation

The starting point for this method is the Schrödinger equation

$$i\hbar\frac{\partial}{\partial t}\left|\Psi(t)\right\rangle = \hat{H}(t)\left|\Psi(t)\right\rangle. \tag{3.23}$$

The Hamiltonian $\hat{H}(t) = \hat{H}_0 + \hat{H}_p(t)$ includes the system part $\hat{H}_0$, see Eq. (2.17), and the probing part $\hat{H}_p$. By combining the Schrödinger equation and the Hamiltonian, it

follows that

$$\begin{aligned} 0 &= \left(\hat{H}_0 + \hat{H}_p(t) - i\hbar\frac{\partial}{\partial t}\right)|\Psi(t)\rangle \\ &= \left(\hat{H}_0 + \hat{H}_p(t) - i\hbar\frac{\partial}{\partial t}\right)\sum_j a_j(t)\,|u_j\rangle\, e^{-iE_jt/\hbar} \\ &= \sum_j \left(a_j(t)\big[E_j + \hat{H}_p(t)\big]\,|u_j\rangle\, e^{-iE_jt/\hbar} - i\hbar\big[\frac{\partial}{\partial t}a_j(t) - \frac{iE_j}{\hbar}a_j(t)\big]\,|u_j\rangle\, e^{-iE_jt/\hbar}\right) \\ &= \sum_j \left(a_j(t)\hat{H}_p(t)\,|u_j\rangle\, e^{-iE_jt/\hbar} - i\hbar\frac{\partial}{\partial t}a_j(t)\,|u_j\rangle\, e^{-iE_jt/\hbar}\right) \end{aligned} \tag{3.24}$$

where we have used the eigenstate decomposition, similar to Eq. (2.2). Here, we multiply Eq. (3.24) with $\langle u_k|$, resulting in the differential equation

$$i\hbar\dot{a}_k(t) = \sum_j a_j(t)\,\langle u_k|\hat{H}_p(t)|u_j\rangle\, e^{i(E_k-E_j)t/\hbar}. \tag{3.25}$$

This result is exact, but further progress requires some approximations.

We make the following approximations:

1. The system starts in an eigenstate $|u_j\rangle$, thus $a_i(0) = 0$ for every $i \neq j$.
2. The probing term $\hat{H}_p$ is very weak, and the time of its effect is short. This motivates the approximation that all weight coefficients $a_i(t)$ stay unchanged for the short period of time.

By applying these approximations, we obtain an integral equation

$$a_k(t) = -\frac{i}{\hbar}\int_0^t \langle u_k|\hat{H}_p(t')|u_j\rangle\, e^{i\omega_{kj}t'}\,dt'. \tag{3.26}$$

In our case the probing term is harmonic, and the easiest harmonic probe to work with is

$$\hat{H}_p(t) = 2\hat{H}_p\cos\omega t = \hat{H}_p\big(e^{-i\omega t} + e^{i\omega t}\big). \tag{3.27}$$

By inserting Eqs. (3.27) to (3.26) we obtain that

$$\begin{aligned} a_k(t) &= -\frac{i\,\langle u_k|\hat{H}_p|u_j\rangle}{\hbar}\int_0^t \big(e^{-i(\omega_{kj}-\omega)t'} + e^{i(\omega_{kj}+\omega)t'}\big)dt' \\ &= -\frac{\langle u_k|\hat{H}_p|u_j\rangle}{\hbar}\left[\frac{e^{-i(\omega_{kj}-\omega)t}-1}{\omega_{kj}-\omega} + \frac{e^{i(\omega_{kj}+\omega)t}-1}{\omega_{kj}+\omega}\right]. \end{aligned} \tag{3.28}$$

If we take a look at Eq. (3.28) we see that for $\omega_{kj} - \omega \simeq 0$ the first term has a significant contribution to $a_k(t)$, and the contribution of the second term is negligible. Thus we

may drop the second term, which results to the transition probability

$$\begin{aligned} \left|a_k(t)\right|^2 &= \frac{\left|\left\langle u_k\middle|\hat{H}_p\middle|u_j\right\rangle\right|^2}{\hbar^2}\left|\frac{e^{-i(\omega_{kj}-\omega)t}-1}{\omega_{kj}-\omega}\right|^2 \\ &= \frac{4\left|\left\langle u_k\middle|\hat{H}_p\middle|u_j\right\rangle\right|^2}{\hbar^2}\frac{\sin^2[(\omega_{kj}-\omega)t/2]}{(\omega_{kj}-\omega)^2}. \end{aligned} \tag{3.29}$$

Here, we employ the relation

$$\lim_{t\to\infty}\frac{\sin^2[tx]}{tx^2} = \pi\delta(x). \tag{3.30}$$

Therefore, the transition probability can be written as

$$\left|a_k(t)\right|^2 = \frac{2\pi\left|\left\langle u_k\middle|\hat{H}_p\middle|u_j\right\rangle\right|^2}{\hbar^2}\delta(\omega_{kj}-\omega)t. \tag{3.31}$$

This is a linear function of time, which means that the transition rate is not time-dependent:

$$\mathcal{P}_{jk}(\omega) = \frac{d}{dt}\left|a_k(t)\right|^2 = \frac{2\pi}{\hbar^2}\left|\left\langle u_k\middle|\hat{H}_p\middle|u_j\right\rangle\right|^2\delta(\omega_{kj}-\omega). \tag{3.32}$$

The result in Eq. (3.32) is often called as Fermi's golden rule. To expand this result to cover every possible transition, we need to sum over every initial and final state, and also assign the probability amplitudes $p_j = \left|a_j\right|^2$ for each initial eigenstate. The result is the following

$$\mathcal{P}(\omega) = \sum_j p_j \sum_k \frac{d}{dt}\left|a_k(t)\right|^2 = \sum_j p_j \sum_k \frac{2\pi}{\hbar^2}\left|\left\langle u_k\middle|\hat{H}_p\middle|u_j\right\rangle\right|^2\delta(\omega_{kj}-\omega). \tag{3.33}$$

However, this result describes transition rates without dissipation, which is valid for the ideal case, but in the presence of dissipation the spectrum is affected by the spectral line broadening that described in Eq. (3.22). Thus, the final result for the absorptive transition rates is

$$\mathcal{P}(\omega) = \frac{1}{\hbar^2}\sum_{if} p_i \frac{\gamma_{if}\left|\left\langle u_f\middle|\hat{H}_p\middle|u_i\right\rangle\right|^2}{(\omega_{fi}-\omega)^2 - \frac{1}{4}\gamma_{if}^2}. \tag{3.34}$$

This line broadening is known as the Wigner-Weisskopf line shape, in which the transition spikes are characterized by Lorentzian distributions instead of δ-functions. Also the result in Eq. (3.34) can be simplified by inserting $\Gamma = \gamma_{if} = \gamma_i + \gamma_f$, where we have summed the decays related to initial and final states [48].

3.2.2 Connection between absorption spectrum and transition rates

We have introduced two approaches to describe the spectrum induced by the probing operator. To make sure that these two results are comparable, we show that the Fermi's golden rule can be derived from the correlation function approach.

The absorption spectrum that is equal to the transition rate function in Eq. (3.34) is

$$S(\omega) = \frac{1}{\hbar^2}\int_{-\infty}^{\infty}\left\langle \hat{H}_p^\dagger(t)\hat{H}_p(0)\right\rangle e^{-i\omega t}dt, \tag{3.35}$$

where $\hat{H}_p$ is presented in the Heisenberg picture [48]. In the following, we go through step by step, how these two approaches are equal:

$$\begin{aligned}
S(\omega) &= \frac{1}{\hbar^2}\int_{-\infty}^{\infty}\left\langle \hat{H}_p^\dagger(t)\hat{H}_p(0)\right\rangle e^{-i\omega t}dt \\
&= \frac{1}{\hbar^2}\int_{-\infty}^{0}\left\langle \hat{H}_p^\dagger(t)\hat{H}_p(0)\right\rangle e^{-i\omega t}dt + \frac{1}{\hbar^2}\int_{0}^{\infty}\left\langle \hat{H}_p^\dagger(t)\hat{H}_p(0)\right\rangle e^{-i\omega t}dt \\
&= -\frac{1}{\hbar^2}\int_{0}^{-(-\infty)}\left\langle \hat{H}_p^\dagger(-t)\hat{H}_p(0)\right\rangle e^{-i\omega(-t)}d(-t) + \frac{1}{\hbar^2}\int_{0}^{\infty}\left\langle \hat{H}_p^\dagger(t)\hat{H}_p(0)\right\rangle e^{-i\omega t}dt \\
&= \frac{1}{\hbar^2}\int_{0}^{\infty}\left\langle \hat{H}_p^\dagger(-t)\hat{H}_p(0)\right\rangle e^{-i\omega(-t)}dt + \frac{1}{\hbar^2}\int_{0}^{\infty}\left\langle \hat{H}_p^\dagger(t)\hat{H}_p(0)\right\rangle e^{-i\omega t}dt.
\end{aligned} \tag{3.36}$$

At this point let us take a closer look to the correlation functions in (3.36):

$$\begin{aligned}
\left\langle \hat{H}_p^\dagger(t)\hat{H}_p(0)\right\rangle &= \mathrm{Tr}\left[\hat{\varrho}e^{i\hat{H}t/\hbar}\hat{H}_p^\dagger(0)e^{-i\hat{H}t/\hbar}\hat{H}_p(0)\right] \\
&= \sum_j\sum_k \left\langle u_j\right|p_k\left|u_k\right\rangle\left\langle u_k\right|e^{i\hat{H}t/\hbar}\hat{H}_p^\dagger(0)e^{-i\hat{H}t/\hbar}\hat{H}_p(0)\left|u_j\right\rangle \\
&= \sum_j\sum_k p_k\left\langle u_j|u_k\right\rangle\left\langle u_k\right|e^{i\hat{H}t/\hbar}\hat{H}_p^\dagger(0)e^{-i\hat{H}t/\hbar}\hat{H}_p(0)\left|u_j\right\rangle \\
&= \sum_j p_j\left\langle u_j\right|e^{i\hat{H}t/\hbar}\hat{H}_p^\dagger(0)e^{-i\hat{H}t/\hbar}\hat{H}_p(0)\left|u_j\right\rangle \\
&= \sum_j\sum_i p_j\left\langle u_j\right|e^{i\hat{H}t/\hbar}\hat{H}_p^\dagger(0)e^{-i\hat{H}t/\hbar}\left|u_i\right\rangle\left\langle u_i\right|\hat{H}_p(0)\left|u_j\right\rangle \\
&= \sum_j\sum_i p_j e^{i(\omega_j-\omega_i)t}\left\langle u_j\right|\hat{H}_p^\dagger(0)\left|u_i\right\rangle\left\langle u_i\right|\hat{H}_p(0)\left|u_j\right\rangle \\
&= \sum_j\sum_i p_j e^{i\omega_{ji}t}\left|\left\langle u_j\right|\hat{H}_p(0)\left|u_i\right\rangle\right|^2
\end{aligned} \tag{3.37}$$

Here, we apply this result to Eq. (3.36), and also assume that the initial probabilities of excited states are decaying exponentially, i.e. $p_j(t) = p_j e^{-\frac{\Gamma}{2}t}$. By combining both parts

in Eq. (3.36) gives us the following:

$$\begin{aligned} S(\omega) &= \sum_{j,i} \frac{\left|\langle u_j|\hat{H}_p(0)|u_i\rangle\right|^2}{\hbar^2} \int_0^\infty p_j e^{-\frac{\Gamma}{2}t}\left[e^{-i(\omega_{ji}-\omega)t} + e^{i(\omega_{ji}-\omega)t}\right]dt \\ &= \sum_{j,i} \frac{\left|\langle u_j|\hat{H}_p(0)|u_i\rangle\right|^2}{\hbar^2} p_j \int_0^\infty e^{-\frac{\Gamma}{2}t} 2\cos\left[(\omega_{ji}-\omega)t\right]dt \\ &= \sum_{j,i} \frac{\left|\langle u_j|\hat{H}_p(0)|u_i\rangle\right|^2}{\hbar^2} p_j \frac{\Gamma}{(\omega_{ji}-\omega)^2 + \frac{1}{4}\Gamma^2}, \end{aligned} \tag{3.38}$$

where the integral is solved by using Laplace transformation. Comparison between results in Eqs. (3.34) and (3.38) shows that, indeed, these two approaches to the problem are equal.

Chapter 4

Physical setup: 1-D transmon array and Bose-Hubbard model

4.1 Bose-Hubbard model

The phenomenon of many-body localization is not bound to any specific physical system. Instead there are many practical solutions to demonstrate MBL. For example, behaviour of electrons in an atomic lattice is approximated by the Hubbard model [49] of Eq. (2.4) and the behaviour of spin excitations in a spin lattice is described by the Heisenberg XXZ model of Eq. (2.5). These are the models that are the most common in the MBL literature, but in this thesis we study a model known as the 1-D Bose-Hubbard model with attractive on-site interactions, which is described by the Hamiltonian

$$\hat{H} = \sum_{i=1}^{L} \omega_i \hat{n}_i - \frac{U}{2} \sum_{i=1}^{L} \hat{n}_i(\hat{n}_i - 1) + J \sum_{i=1}^{L-1} (\hat{b}_i^\dagger \hat{b}_{i+1} + \hat{b}_{i+1}^\dagger \hat{b}_i), \tag{4.1}$$

where $\hat{n}_i$ and $\hat{b}_i$ refer to the number and annihilation operators at site i. In this case, the operators $\hat{b}_i$ and $\hat{b}_i^\dagger$ are bosonic operators and, thus, they obey the commutation relation $\left[\hat{b}_i, \hat{b}_j^\dagger\right] = \delta_{ij}$. If one would have fermions instead of bosons (for example the Hubbard model), the creation and annihilation operators would obey the anti-commutation relation $\left\{\hat{b}_i, \hat{b}_j^\dagger\right\} = \delta_{ij}$. Total number of sites is given by L. We also assume that $\hbar = 1$.

Bose-Hubbard Hamiltonian (4.1) is very similar to the Hubbard model in Eq. (2.4), only difference being that the Bose-Hubbard model describes bosons instead of fermions. Even though the Hamiltonians seem similar, there is a critical distinction in the behaviour of fermions and bosons. Fermions are affected by the Pauli exclusion principle,

which prohibits identical fermions from occupying the same quantum state [9], and therefore the eigenvalues for number operators are $n_i = 0, 1$ for spinless fermions. On the other hand, bosons do not have this restriction, which means that the possible eigenvalues for the number operator are $n_i = 0, 1, ..., N$, where N is the total number of excitations in the system. It is clear that the size of the Hilbert space grows much faster as a function of N in the case of the Bose-Hubbard model compared to the Hubbard model. The larger size of the Hilbert space of Bose-Hubbard model makes it increasingly more difficult to do numerical modelling on these MBL systems, which is one of the reasons why many numerical papers prefer to study MBL in the context of Hubbard and Heisenberg models. However, there are some studies concentrating on the numerical modelling of Bose-Hubbard chain e.g. in Refs. [50, 51].

There has been a significant development in experimental quantum systems which fall into the category of Bose-Hubbard models. One such experimental system is cold atoms in an optical lattice [52], which has been recently utilized to demonstrate MBL experimentally in two dimensions [53]. Another system that has been studied recently in the context of MBL [6] is made of superconducting quantum circuits [54].

The superconducting quantum circuits have gained much attention, in recent decades, because they offer a promising platform to store and process quantum information coherently. This feature makes superconducting circuits a promising candidate to build quantum bits (also known as qubits), which could be used to build a quantum computer [55–57]. The most promising superconducting circuit design from the perspective of coherence times is known as the transmon qubit [58, 59].

These transmon qubits act as a basic building block of the Bose-Hubbard system studied in this thesis. In the following sections, we shortly introduce the physics of transmon qubits and the connection with the Bose-Hubbard model.

4.2 Transmon qubit

Transmon qubits are a part of a more general design of qubits, known as superconducting qubits. Other well-known members of this design are e.g. phase, flux and charge qubits, which all predate the transmons [54, 55, 57]. All of them have their own circuit designs and/or parameter sweet-spots, but one important common feature for all superconducting qubits is the use of quantum mechanical circuit element called the Josephson junction [60]. See the circuit diagram symbol for the Josephson junction in Fig. 4.1.

Josephson junction is a superconducting circuit element, which has two superconducting electrodes separated by a thin insulating layer. In a classical situation, no current

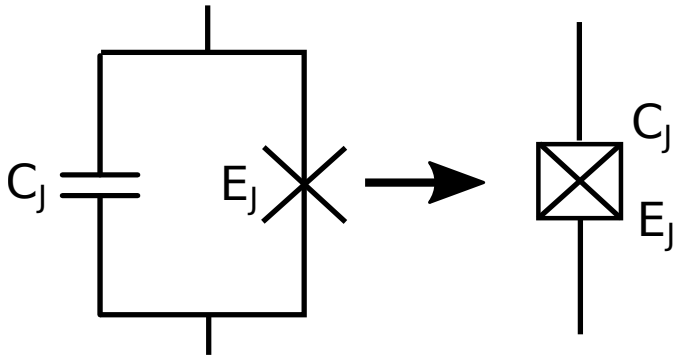

FIGURE 4.1: Circuit diagram symbols for the Josephson junction. The diagram on the left describes the Josephson tunnel element (symbol X) and the capacitance separately. Usually this is simplified with symbol presented on the right side, which is usually referred as the Josephson junction.

through the insulating layer is allowed. On the other hand, in the case of superconductors, there is a current consisting of Cooper pairs, enabled by the quantum tunneling effect. The transmon is made of a Josephson junction shunted with capacitor plates and it can be seen as an anharmonic electric oscillator, that is, a nonlinear LC circuit. The tunneling Cooper pairs of the Josephson junction create a nonlinear kinetic inductance [55]. The nonlinearity plays a critical role if these circuits are used as qubits, since it decreases the energy difference between neighbouring energy levels as the absolute energy of the energy level increases. Because of this, it is possible to isolate the ground state and 1. excited state from the rest of the energy levels. If we limit the system to occupy only two lowest energy levels, we can treat it as an effective two-state system.

The closest relative of the transmon qubit is the charge qubit, which has an almost identical circuit diagram. Both have the Cooper pair box as a basic structure, transmon qubit has one additional shunting capacitance, which increases the ratio of Josephson energy E_J and charge energy E_C i.e. E_J/E_C increases [58]. This decreases significantly the charge dispersion of the qubit, while anharmonicity is also decreased. However, it is possible to find optimal parameter regime $25 \lesssim E_J/E_C \lesssim 100$, where the charge dispersion becomes insignificant, but the anharmonicity remains large enough to allow qubit operations [58].

4.2.1 Derivation of 1-D transmon array Hamiltonian

In the following, we use the theory of quantum electromagnetic circuits, introduced in Ref. [54], to construct the Hamiltonian for transmon qubits in a one-dimensional chain. The coupling between qubits is capacitive, and only nearest neighbour couplings are assumed to be significant [61]. The electric circuit diagram for such system is presented in Fig. 4.2.

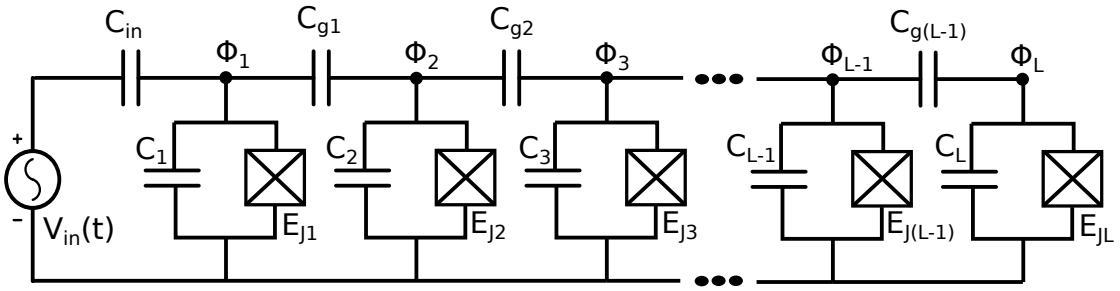

FIGURE 4.2: Electric circuit diagram for 1-D capacitively coupled transmon qubit array with capacitively coupled external voltage source. Symbol L denotes the length of the array. The Lagrangian for this system is presented in Eqs. (4.2), (4.3) and (4.4).

The classical Hamiltonian function of the transmon array can be derived by forming the Lagrangian function of the system by using the methods explained in Ref. [54]. The Lagrangian function of an array of L capacitively-coupled transmons is

$$\mathcal{L} = T - V, \tag{4.2}$$

where

$$T = \sum_{i=1}^{L} \frac{1}{2} C_i \dot{\Phi}_i^2 + \sum_{i=1}^{L-1} \frac{1}{2} C_{g_i} (\dot{\Phi}_{i+1} - \dot{\Phi}_i)^2 + \frac{1}{2} C_{\text{in}} [\dot{\Phi}_k - V_{\text{in}}(t)]^2 \tag{4.3}$$

is the kinetic energy part, and

$$V = -\sum_{i=1}^{L} E_{J_i} \cos\left(2\pi \frac{\Phi_i}{\Phi_0}\right) \tag{4.4}$$

is the potential energy part, where Φ_0 is the magnetic flux quantum. Here, the degrees of freedom are the node fluxes Φ_i, and we have also assumed that a time-depended drive $V_{\text{in}}(t)$ is coupled to the k-site through the capacitance C_{in} (in Fig. 4.2, the drive is coupled to the first site but, in general, the drive can be coupled to any site). Also, the Josephson capacitances C_{J_i} and shunting capacitances C_{B_i} are lumped into the capacitance $C_i = C_{J_i} + C_{B_i}$.

We know from classical mechanics [62], that a Lagrangian function $\mathcal{L}$ can be transformed to a corresponding Hamiltonian function $\mathcal{H}$ by using the Legendre transformation

$$\mathcal{H} = \sum_{i=1}^{L} Q_i \dot{\Phi}_i - \mathcal{L}, \tag{4.5}$$

and the change to canonical variables $(\Phi_i, \dot{\Phi}_i) \to (\Phi_i, Q_i)$ is achieved with the equation

$$Q_i = \frac{\partial \mathcal{L}}{\partial \dot{\Phi}_i} = C_i \dot{\Phi}_i + C_{g_i}(\dot{\Phi}_i - \dot{\Phi}_{i-1}) - C_{\text{in}}(\dot{\Phi}_{i+1} - \dot{\Phi}_i) + C_{g_i}[\dot{\Phi}_k - V_{\text{in}}(t)]\delta_{ki}. \tag{4.6}$$

The transformation is much easier to perform using matrix representation. Thus, we will define the following matrix and vectors:

$$\boldsymbol{\mathcal{C}} = \begin{bmatrix} C_1 + C_{g_1} & -C_{g_1} & \dots & 0 \\ -C_{g_1} & C_{g_1} + C_2 + C_{g_2} & \dots & 0 \\ \vdots & & \ddots & \vdots \\ 0 & & \dots & C_{g_{L-1}} + C_L \end{bmatrix}, \boldsymbol{\Phi} = \begin{bmatrix} \Phi_1 \\ \Phi_2 \\ \vdots \\ \Phi_L \end{bmatrix}, \boldsymbol{\mathcal{Q}} = \begin{bmatrix} Q_1 \\ Q_2 \\ \vdots \\ Q_L \end{bmatrix},$$

where $\mathcal{C}$ is a symmetric tridiagonal capacitance matrix. In the case of external drive, it is useful to define the vector

$$\boldsymbol{a} = \begin{bmatrix} 0 \\ \vdots \\ C_{\text{in}} V_{\text{in}} \\ \vdots \\ 0 \end{bmatrix},$$

where only the element number k is non-zero. Also, one needs to add the capacitance C_{in} into the k^{th} diagonal element of matrix $\boldsymbol{\mathcal{C}}$. Thus, the Lagrangian can be expressed with a simple matrix equation

$$\mathcal{L} = \frac{1}{2}\dot{\boldsymbol{\Phi}}^T \boldsymbol{\mathcal{C}} \dot{\boldsymbol{\Phi}} - \boldsymbol{a}^T \dot{\boldsymbol{\Phi}} - V, \tag{4.7}$$

where the superscript T denotes a transpose. Similarly, the matrix equation for relation in Eq. (4.6) is given by

$$\boldsymbol{\mathcal{Q}} = \boldsymbol{\mathcal{C}} \dot{\boldsymbol{\Phi}} - \boldsymbol{a}. \tag{4.8}$$

More useful form of this equation is

$$\dot{\boldsymbol{\Phi}} = \boldsymbol{\mathcal{C}}^{-1}(\boldsymbol{\mathcal{Q}} + \boldsymbol{a}), \tag{4.9}$$

where the superscript -1 denotes the matrix inverse. By using Eqs. (4.5), (4.7) and (4.9) we obtain a matrix equation for the Hamiltonian function

$$\begin{aligned} \mathcal{H} &= \boldsymbol{\mathcal{Q}}^T \dot{\boldsymbol{\Phi}} - \mathcal{L} \\ &= \boldsymbol{\mathcal{Q}}^T \boldsymbol{\mathcal{C}}^{-1}(\boldsymbol{\mathcal{Q}} + \boldsymbol{a}) - \frac{1}{2}(\boldsymbol{\mathcal{C}}^{-1}(\boldsymbol{\mathcal{Q}} + \boldsymbol{a}))^T \boldsymbol{\mathcal{C}} \boldsymbol{\mathcal{C}}^{-1}(\boldsymbol{\mathcal{Q}} + \boldsymbol{a}) + \boldsymbol{a}^T \boldsymbol{\mathcal{C}}^{-1}(\boldsymbol{\mathcal{Q}} + \boldsymbol{a}) + V \\ &= \frac{1}{2}(\boldsymbol{\mathcal{Q}} + \boldsymbol{a})^T \boldsymbol{\mathcal{C}}^{-1}(\boldsymbol{\mathcal{Q}} + \boldsymbol{a}) + V \\ &= \frac{1}{2}(\boldsymbol{\mathcal{Q}} + \boldsymbol{a})^T \boldsymbol{\mathcal{C}}^{-1}(\boldsymbol{\mathcal{Q}} + \boldsymbol{a}) - \sum_{i=1}^{L} E_{J_i} \cos\left(2\pi \frac{\Phi_i}{\Phi_0}\right). \end{aligned} \tag{4.10}$$

Eq. (4.10) is the exact Hamiltonian of the system. Working with the exact Hamiltonian

becomes complicated if the length of the array L is large and, thus, we prefer to make reasonable approximations.

The first approximation focuses on the inverse of the capacitance matrix $\boldsymbol{\mathcal{C}^{-1}}$. We assume that the coupling capacitances are small compared to the transmon capacitances, i.e. $C_{g_i} \ll C_j, \forall\, i, j$. In the first order in C_{g_i}/C_j, this leads to the matrix elements

$$\begin{aligned}
(\mathcal{C}^{-1})_{ii} &= \frac{1}{\mathcal{C}_{ii}} = \frac{1}{C_i + C_{g_{i-1}} + C_{g_i}},\ i \neq k, \\
(\mathcal{C}^{-1})_{kk} &= \frac{1}{\mathcal{C}_{kk}} = \frac{1}{C_k + C_{g_{k-1}} + C_{g_k} + C_{\text{in}}}, \\
(\mathcal{C}^{-1})_{i,i+1} &= -\frac{(\mathcal{C})_{i,i+1}}{(\mathcal{C})_{i,i}(\mathcal{C})_{i+1,i+1}} = \frac{C_{g_i}}{\big(C_i + C_{g_{i-1}} + C_{g_i}\big)\big(C_{i+1} + C_{g_i} + C_{g_{i+1}}\big)}.
\end{aligned} \tag{4.11}$$

The formula for exact matrix elements for an inverse of a tridiagonal matrix is presented in Ref. [63].

The second approximation focuses on the potential energy term V. We make a Taylor expansion for the cosine term with respect to the variable Φ_i. By assuming small phase fluctuations, and large E_J/E_C, we neglect terms with higher order than four in Φ_i [58]. This results to the potential energy

$$V \approx -\sum_{i=1}^{L} E_{J_i}\left[1 - \frac{1}{2}\left(\frac{2e}{\hbar}\Phi\right)^2 + \frac{1}{24}\left(\frac{2e}{\hbar}\Phi\right)^4\right], \tag{4.12}$$

where we have used the magnetic flux quantum $\Phi_0 = h/(2e)$. The constant term in Eq. (4.12) is not relevant and therefore we can drop it.

These approximations allow us to express the Hamiltonian function as

$$\mathcal{H} = \mathcal{H}_0 + \mathcal{H}_1 + \mathcal{H}_2 + \mathcal{H}_3. \tag{4.13}$$

The first term describes a harmonic oscillator part of the system

$$\mathcal{H}_0 = \sum_{i=1}^{L}\left[\frac{Q_i^2}{2(\mathcal{C})_{ii}} + \frac{\Phi_i^2}{2L_i}\right], \tag{4.14}$$

where we have used the effective inductance, defined as $L_i = \hbar^2/(4E_{J_i}e^2)$. The second term describes the anharmonicity that is added to harmonic part $\mathcal{H}_0$ given by

$$\mathcal{H}_1 = -\sum_{i=1}^{L}\frac{2E_{J_i}e^4}{\hbar^4}\Phi_i^4. \tag{4.15}$$

The third term expresses the couplings between qubits as

$$\mathcal{H}_2 = \sum_{i=1}^{L-1} -\frac{(\mathcal{C})_{i,i+1}}{(\mathcal{C})_{i,i}(\mathcal{C})_{i+1,i+1}} Q_i Q_{i+1} \tag{4.16}$$

The last term $\mathcal{H}_3$ couples the driving voltage V_{in} to qubits:

$$\mathcal{H}_3 = \sum_{i=1}^{L} C_{\text{in}} V_{\text{in}}(t)(\mathcal{C}^{-1})_{i,k} Q_i. \tag{4.17}$$

Lastly, we note that constant terms without any couplings to canonical variables $\{\Phi_i, Q_i\}$ are neglected.

4.2.2 Quantum picture

We have constructed the classical Hamiltonian function for the capacitively coupled transmon array with a classical drive in Eq. (4.13). Naturally, the next step is to move into the quantum picture. Here, one should note that for our purposes it is enough to quantize only the degrees of freedom describing the qubits, and leave the external drive into the classical form.

The quantization of the variables $\{\Phi_i, Q_i\}$ is very similar to the case of the simple harmonic oscillator with the canonical variables x and p [13]. We replace the set of canonical variables with operators, $\{\Phi_i, Q_i\} \to \{\hat{\Phi}_i, \hat{Q}_i\}$, which follow the commutation relation [54]

$$[\hat{\Phi}_i, \hat{Q}_i] = i\hbar. \tag{4.18}$$

In the quantum picture, it is much easier to work with the creation and annihilation operators which are defined as [54]

$$\hat{\Phi}_i = \sqrt{\frac{\hbar Z_i}{2}}(\hat{b}_i + \hat{b}_i^\dagger) \tag{4.19}$$

and

$$\hat{Q}_i = \frac{1}{i}\sqrt{\frac{\hbar}{2Z_i}}(\hat{b}_i - \hat{b}_i^\dagger), \tag{4.20}$$

where the effective impedance is denoted as $Z_i = \sqrt{L_i/(\mathcal{C})_{ii}}$. Creation and annihilation operators follows the familiar commutation relation

$$[\hat{b}_i, \hat{b}_j^\dagger] = \delta_{ij}. \tag{4.21}$$

4.2.3 Connection to Bose-Hubbard model

At this point, we are ready to show how the quantized version of the transmon array Hamiltonian (4.13) is connected to the Bose-Hubbard Hamiltonian (4.1). We address the quantized version of the harmonic oscillator part in Eq. (4.14) and apply the Eqs. (4.19) and (4.20), resulting in

$$\begin{aligned}\hat{H}_0 &= \sum_{i=1}^{L}\left[\frac{\hat{Q}_i^2}{2(\mathcal{C})_{ii}} + \frac{\hat{\Phi}_i^2}{2L_i}\right] \\ &= \sum_{i=1}^{L}\frac{\hbar}{4}\omega_i^{'}\big[-(\hat{b}_i\hat{b}_i + \hat{b}_i^{\dagger}\hat{b}_i^{\dagger} - \hat{b}_i\hat{b}_i^{\dagger} - \hat{b}_i^{\dagger}\hat{b}_i) + (\hat{b}_i\hat{b}_i + \hat{b}_i^{\dagger}\hat{b}_i^{\dagger} + \hat{b}_i\hat{b}_i^{\dagger} + \hat{b}_i^{\dagger}\hat{b}_i)\big] \\ &= \sum_{i=1}^{L}\frac{\hbar}{2}\omega_i^{'}\big(\hat{b}_i^{\dagger}\hat{b}_i + \hat{b}_i\hat{b}_i^{\dagger}\big) = \sum_{i=1}^{L}\hbar\omega_i^{'}\left(\hat{b}_i^{\dagger}\hat{b}_i + \frac{1}{2}\right),\end{aligned} \tag{4.22}$$

where we have defined $\omega_i^{'} = \sqrt{\frac{1}{(\mathcal{C})_{ii}L_i}}$.

Here, we consider the quantized anharmonic part of the oscillator in Eq. (4.15)

$$\begin{aligned}\hat{H}_1 &= -\sum_{i=1}^{L}\frac{2E_{J_i}e^4}{\hbar^4}\hat{\Phi}_i^4 = -\sum_{i=1}^{L}\frac{2E_{J_i}e^4}{\hbar^4}\frac{\hbar^2 L_i}{4(\mathcal{C})_{ii}}\big(\hat{b}_i + \hat{b}_i^{\dagger}\big)^4 \\ &= -\sum_{i=1}^{L}\frac{1}{24}\frac{e^2}{(\mathcal{C})_{ii}}\big(\hat{b}_i + \hat{b}_i^{\dagger}\big)^4 = -\sum_{i=1}^{L}\frac{E_{C_i}}{12}\big(\hat{b}_i + \hat{b}_i^{\dagger}\big)^4,\end{aligned} \tag{4.23}$$

where $E_{C_i} = e^2/(2(\mathcal{C})_{ii})$ is the charging energy. We approximate the operator $\big(\hat{b}_i + \hat{b}_i^{\dagger}\big)^4$ by neglecting the terms which change the number of excitations in the system, that is, we take into account its effect only in the first order of the non-degenerate perturbation theory. We obtain the following Hamiltonian:

$$\hat{H}_1 \approx -\sum_{i=1}^{L}\frac{E_{C_i}}{12}\Big[6\big(\hat{b}_i^{\dagger}\hat{b}_i\big)^2 + 6\hat{b}_i^{\dagger}\hat{b}_i + 3\Big] = -\sum_{i=1}^{L}\frac{E_{C_i}}{2}\Big[\hat{n}_i^2 + \hat{n}_i + \frac{1}{2}\Big], \tag{4.24}$$

where $\hat{n}_i = \hat{b}_i^{\dagger}\hat{b}_i$ is the number operator for the site i. Again, we ignore the constant term, and after straightforward algebra we obtain

$$\begin{aligned}\hat{H}_1 &= -\sum_{i=1}^{L}\frac{E_{C_i}}{2}\Big[\hat{n}_i^2 + \hat{n}_i\Big] = -\sum_{i=1}^{L}\frac{E_{C_i}}{2}\Big[\hat{n}_i^2 - \hat{n}_i + 2\hat{n}_i\Big] \\ &= -\sum_{i=1}^{L}\frac{E_{C_i}}{2}\hat{n}_i\big(\hat{n}_i - 1\big) + \sum_{i=1}^{L}E_{C_i}\hat{n}_i.\end{aligned} \tag{4.25}$$

The first sum in Eq. (4.25) corresponds to the on-site interaction term in the Bose-Hubbard model in Eq. (4.1). Thus, we move the second sum into the harmonic oscillator part $\hat{H}_0$ and redefine the natural frequency as $\omega_i = \omega_i^{'} - E_{C_i}/\hbar$. This leads to

$$\hat{H}_0 + \hat{H}_1 = \sum_{i=1}^{L} \hbar\omega_i \hat{n}_i - \sum_{i=1}^{L} \frac{E_{C_i}}{2} \hat{n}_i\big(\hat{n}_i - 1\big), \tag{4.26}$$

where the constant term corresponding to zero-point fluctuations is dropped. By comparing Eq. (4.26) to the Bose-Hubbard model in Eq. (4.1), we observe that the connection to on-site interaction parameter is

$$U_i = \frac{E_{C_i}}{\hbar}. \tag{4.27}$$

Here, we focus on the part $\hat{H}_2$, which corresponds to the hopping term of the Bose-Hubbard model in Eq. (4.1). We use the relations in Eqs. (4.20) and (4.21). Also, we neglect the terms which break the excitation number symmetry i.e. $\hat{b}_i\hat{b}_{i+1}$ and $\hat{b}_i^\dagger\hat{b}_{i+1}^\dagger$. This results into the following Hamiltonian:

$$\begin{aligned}
\hat{H}_2 &= \sum_{i=1}^{L-1} -\frac{(\mathcal{C})_{i,i+1}}{(\mathcal{C})_{i,i}(\mathcal{C})_{i+1,i+1}} \hat{Q}_i\hat{Q}_{i+1} \\
&= \sum_{i=1}^{L-1} -\frac{(\mathcal{C})_{i,i+1}}{(\mathcal{C})_{i,i}(\mathcal{C})_{i+1,i+1}} \frac{1}{i}\sqrt{\frac{\hbar}{2Z_i}}(\hat{b}_i - \hat{b}_i^\dagger)\frac{1}{i}\sqrt{\frac{\hbar}{2Z_{i+1}}}(\hat{b}_{i+1} - \hat{b}_{i+1}^\dagger) \\
&= \sum_{i=1}^{L-1} -\frac{\hbar}{2}\frac{(\mathcal{C})_{i,i+1}}{(\mathcal{C}_{i,i}\mathcal{C}_{i+1,i+1})^{3/4}(L_iL_{i+1})^{1/4}}(\hat{b}_i^\dagger\hat{b}_{i+1} + \hat{b}_{i+1}^\dagger\hat{b}_i).
\end{aligned} \tag{4.28}$$

We have, thus, shown that the connection to the Bose-Hubbard models hopping parameter is the following:

$$J_i = -\frac{1}{2}\frac{(\mathcal{C})_{i,i+1}}{(\mathcal{C}_{i,i}\mathcal{C}_{i+1,i+1})^{3/4}(L_iL_{i+1})^{1/4}}, \tag{4.29}$$

where J_i is positive because $(\mathcal{C})_{i,i+1} = -C_{g_i}$.

The capacitively coupled external drive is described by the quantized version of Eq. (4.17), which is the following:

$$\hat{H}_3 = \sum_{i=1}^{L} C_{\text{in}}V_{\text{in}}(t)(\mathcal{C}^{-1})_{i,k}\hat{Q}_i = \sum_{i=1}^{L} \frac{1}{i}\sqrt{\frac{\hbar}{2Z_i}} C_{\text{in}}V_{\text{in}}(t)(\mathcal{C}^{-1})_{i,k}(\hat{b}_i - \hat{b}_i^\dagger). \tag{4.30}$$

In this semi-classical approach, where the drive is described classically, the number of excitations is not conserved, as the operator $(\hat{b}_i - \hat{b}_i^\dagger)$ clearly shows.

In previous chapter, it was discussed how Fermi's golden rule could be used to determine a transition rate spectrum under weak external drive, and how certain signatures can

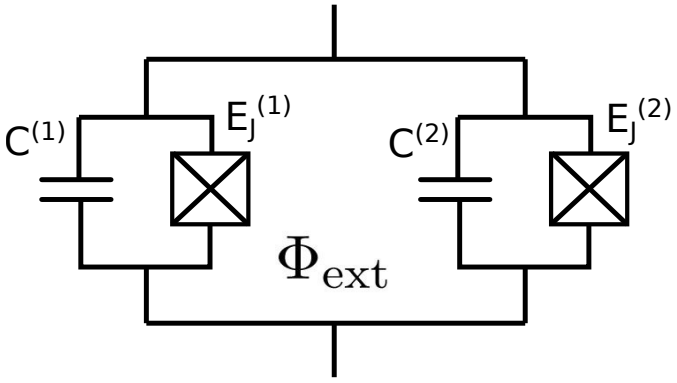

FIGURE 4.3: Electric circuit diagram for two parallel Josephson junctions. By applying a time-dependent external magnetic flux Φ_{ext} through the loop, one can drive the transmon qubit array without changing the number of excitations.

point out the dynamical phase of the system. The main signature of MBL was a smooth gap at $\omega = 0$, known as soft gap. The concept of the soft gap is meaningful only if transitions conserve the excitation number, since the transitions to lower or higher symmetry sectors generally have large energy differences between the initial and the final state.

In the following subsection, a new external drive is introduced, which does not cause transitions to different symmetry sectors but, instead, conserves the excitation number.

4.2.4 Driving transmon with magnetic flux

Hitherto, we have assumed that a transmon qubit has only one Josephson junction with parallelly coupled capacitors C_J and C_B, but in general transmon qubits can be build to have two parallel Josephson junctions, $E_J^{(1)}$ and $E_J^{(2)}$, with parallel capacitances $C_J^{(1)}$, $C_J^{(2)}$ and C_B. These two parallel Josephson junctions form a loop, which means that the effective Josephson energy is dependent on the magnetic flux Φ_{ext} going through the loop [64]. The loop made of two parallel Josephson junctions is presented in Fig. 4.3.

The new Hamiltonian corresponding to the two parallel Josephson elements of the transmon qubit is

$$\hat{H}_J = -E_J^{(1)} \cos\hat{\phi}_1 - E_J^{(2)} \cos\hat{\phi}_2, \tag{4.31}$$

where $\hat{\phi}_1 = 2\pi\frac{\hat{\Phi}^{(1)}}{\Phi_0}$ and $\hat{\phi}_2 = 2\pi\frac{\hat{\Phi}^{(2)}}{\Phi_0}$. In addition we use the following relation [58]

$$\phi_1 - \phi_2 = 2\pi n + 2\pi\frac{\Phi_{\text{ext}}}{\Phi_0}, \tag{4.32}$$

where n is an integer and Φ_{ext} is the external magnetic flux piercing the loop. We also define the variables $\phi = (\phi_1 + \phi_2)/2$, $E_{J\Sigma} = E_J^{(1)} + E_J^{(2)}$, and $d = \frac{E_J^{(2)} - E_J^{(1)}}{E_J^{(1)} + E_J^{(2)}}$. By using

these relations, we express the Hamiltonian (4.31) in the following form [58]:

$$\begin{aligned}\hat{H}_J &= -E_{J\Sigma}\left[\cos\left(\frac{\pi\Phi_{\text{ext}}}{\Phi_0}\right)\cos\hat{\phi} + d\sin\left(\frac{\pi\Phi_{\text{ext}}}{\Phi_0}\right)\sin\hat{\phi}\right] \\ &= -E_{J\Sigma}\cos\left(\frac{\pi\Phi_{\text{ext}}}{\Phi_0}\right)\sqrt{1+d^2\tan^2\left(\frac{\pi\Phi_{\text{ext}}}{\Phi_0}\right)}\cos\left(\hat{\phi}-\phi_0\right),\end{aligned} \tag{4.33}$$

where we have defined $\tan\phi_0 = d\tan\left(\pi\Phi_{\text{ext}}/\Phi_0\right)$.

The relevant differences between the transmon with two junctions in Eq. (4.33) compared to the transmon with one junction in Eq. (4.4) is that in the former the Josephson energy is dependent on the external magnetic flux, i.e.

$$E_J(\Phi_{\text{ext}}) = E_{J\Sigma}\cos\left(\frac{\pi\Phi_{\text{ext}}}{\Phi_0}\right)\sqrt{1+d^2\tan^2\left(\frac{\pi\Phi_{\text{ext}}}{\Phi_0}\right)}, \tag{4.34}$$

and also the cosine term has an additional phase factor dependent on magnetic flux Φ_{ext}. However by assuming that the separate junctions have an almost identical Josephson energies, i.e. $E_J^{(1)} \approx E_J^{(2)}$, the phase factor ϕ_0 becomes negligible. By using the same assumption, we argue that the tangent term in Eq. (4.34) is also irrelevant and, thus, we obtain

$$E_J(\Phi_{\text{ext}}) \approx E_{J\Sigma}\cos\left(\frac{\pi\Phi_{\text{ext}}}{\Phi_0}\right), \tag{4.35}$$

The loop created by the two Josephson junctions creates a new channel to influence the transmon Hamiltonian with the magnetic field. Moreover, this channel allows one to drive the transmon qubit without changing the total number of excitations in the system which was the problem with the capacitively-driven transmon qubit.

In order to show this, we assume that the external magnetic field is time-dependent, and it can be separated into constant and time-dependent terms. We also assume that the time-dependence is harmonic, and given by

$$\frac{\pi}{\Phi_0}\Phi_{\text{ext}}(t) = \frac{\pi}{\Phi_0}\Phi_{\text{dc}} + \frac{\pi}{\Phi_0}\Phi_{\text{ac}}(t) = \alpha + \beta(t) = \alpha + \beta\cos\omega t. \tag{4.36}$$

Further on, we assume that the oscillating part of the drive is weak, that is $\beta \ll 1$. Applying Eq. (4.36) to Eq. (4.35) and using the assumption $\beta \ll 1$, which implies $\sin\left[\beta(t)\right] \approx 0$, we obtain an approximate result

$$\begin{aligned}E_J(t) &= E_{J\Sigma}\cos\left[\alpha + \beta\cos\left(\omega t\right)\right] \\ &= E_{J\Sigma}\left\{\cos(\alpha)\cos\left[\beta\cos\left(\omega t\right)\right] + \sin(\alpha)\sin\left[\beta\cos\left(\omega t\right)\right]\right\} \\ &\approx E_{J\Sigma}\cos(\alpha)\cos\left[\beta\cos\left(\omega t\right)\right]\end{aligned} \tag{4.37}$$

The time-independent factor can be included into the factor $E_{J\Sigma}$, which leads to

$$E_J(t) = E_{J\Sigma} \cos\big[\beta \cos(\omega t)\big]. \tag{4.38}$$

The time-dependence of Josephson energy still looks quite complicated, but here one can utilize a series expansion known as the Jacobi-Anger expansion [65]:

$$\cos\big[\beta \cos(\omega t)\big] = \mathcal{J}_0(\beta) + 2\sum_{n=1}^{\infty}(-1)^n \mathcal{J}_{2n}(\beta) \cos\big(2n\omega t\big), \tag{4.39}$$

where the Bessel functions of the first kind are denoted as $\mathcal{J}_n$. For $\beta \ll 1$ it is good approximation to include only the first two terms in the expansion, which leads to a following form for the Josephson energy

$$E_J(t) \approx E_{J\Sigma}\big[\mathcal{J}_0(\beta) - 2\mathcal{J}_2(\beta) \cos\big(2\omega t\big)\big]. \tag{4.40}$$

4.2.5 Transmon Hamiltonian with magnetic flux drive

The new relation for the Josephson energy is displayed in Eq. (4.40). To see how this couples to the original transmon Hamiltonian, the original Josephson energy of the driven transmon needs to be replaced with Eq. (4.40). This constant clearly appears in the harmonic oscillator part $\hat{H}_0$, and in $\hat{H}_2$ which is the coupling term between qubits.

The harmonic part can be expressed explicitly using E_J [58]. After inserting Eq. (4.40), we obtain the following harmonic part for the driven qubit:

$$\hat{H}_\alpha = \sqrt{8E_C E_{J\Sigma}\big[\mathcal{J}_0(\beta) - 2\mathcal{J}_2(\beta) \cos\big(2\omega t\big)\big]}\,\hat{n}. \tag{4.41}$$

We perform a Taylor approximation with respect to the time-dependent term inside the square root, at zero. By keeping the first two terms, we obtain

$$\hat{H}_\alpha \approx \sqrt{8E_C E_{J\Sigma}}\Big[1 - \mathcal{J}_2(\beta) \cos\big(2\omega t\big)\Big]\hat{n}, \tag{4.42}$$

where it is assumed that $\sqrt{\mathcal{J}_0(\beta)} \simeq 1$.

In the case of a transmon array, the time-dependent Josephson energy appears also in the coupling terms which connect the neighbouring qubits. By replacing the Josephson

energy with Eq. (4.40), we obtain

$$\begin{aligned}\hat{H}_\beta &= -e\frac{(\mathcal{C})_{i,i+1}}{(\mathcal{C}_{i,i}\mathcal{C}_{i+1,i+1})^{3/4}}(E_{J_i}E_{J\Sigma_{i+1}}\left[\mathcal{J}_0(\beta)-2\mathcal{J}_2(\beta)\cos\left(2\omega t\right)\right])^{1/4}(\hat{b}_i^\dagger\hat{b}_{i+1}+\hat{b}_{i+1}^\dagger\hat{b}_i)\\ &\approx -e\frac{(E_{J_i}E_{J\Sigma_{i+1}})^{1/4}(\mathcal{C})_{i,i+1}}{(\mathcal{C}_{i,i}\mathcal{C}_{i+1,i+1})^{3/4}}\left[1-\frac{1}{2}\mathcal{J}_2(\beta)\cos\left(2\omega t\right)\right](\hat{b}_i^\dagger\hat{b}_{i+1}+\hat{b}_{i+1}^\dagger\hat{b}_i),\end{aligned} \tag{4.43}$$

where we have used a similar Taylor approximation as in Eq. (4.42).

In the Hamiltonians (4.42) and (4.43), there are constant and time-dependent parts. In the constant parts there are no significant changes compared to the one-junction case. Thus, because of aesthetic reasons, we include all changes into the parameter E_{J_i}. This means that the time-independent part of the Hamiltonian is still $\hat{H}_0+\hat{H}_1+\hat{H}_2$, as defined in Eqs. (4.26) and (4.28). The time-dependent parts of the full Hamiltonian are a weak perturbations, which we denote as

$$\hat{H}_{p1}=\hbar\omega_k\mathcal{J}_2(\beta)\cos\left(2\omega t\right)\hat{n}_k, \tag{4.44}$$

and

$$\begin{aligned}\hat{H}_{p2} &= -\sum_{i=k-1}^{k}\frac{\hbar}{4}\frac{(\mathcal{C})_{i,i+1}}{(\mathcal{C}_{i,i}\mathcal{C}_{i+1,i+1})^{3/4}(L_iL_{i+1})^{1/4}}\mathcal{J}_2(\beta)\cos\left(2\omega t\right)(\hat{b}_i^\dagger\hat{b}_{i+1}+\hat{b}_{i+1}^\dagger\hat{b}_i)\\ &= \sum_{i=k-1}^{k}\frac{\hbar J_i}{2}\mathcal{J}_2(\beta)\cos\left(2\omega t\right)(\hat{b}_i^\dagger\hat{b}_{i+1}+\hat{b}_{i+1}^\dagger\hat{b}_i).\end{aligned} \tag{4.45}$$

4.2.6 Implementing disorder with magnetic flux

One possible way to realize the disorder, required by the MBL, with transmon chain is to generate different-sized Josephson junction loops for each transmon. Obviously, this leads to different amounts of magnetic flux penetrating each loop, even if the magnetic field is uniform.

As we noticed above, the disorder implemented through external magnetic flux affects the Josephson energy of the transmon. Therefore, the natural frequency of the transmon is changed, as needed to realize MBL, but also the hopping interaction in Eq. (4.29) is varied. This could be problematic since W/J is used as an order parameter for the MBL transition. Fortunately, one can show that the ratio between the disorder in the natural frequency and hopping interaction scales approximately as

$$\frac{\Delta\omega_i}{\Delta J_i}\propto\frac{E_{J_i}}{E_{C_i}}, \tag{4.46}$$

which means that the disorder in ω_i is much more relevant compared to J_i if $E_{J_i}/E_{C_i} \gg 1$. This happens to be one of the defining characteristics of the transmon qubit according to Ref. [58]. Because of this, we neglect the disorder component appearing in the hopping interaction parameter.

4.3 Fermi's golden rule for harmonic magnetic flux perturbation

The perturbing Hamiltonians $\hat{H}_{p1}$ and $\hat{H}_{p2}$ have harmonic time-dependence and the number of excitations in the system is conserved. This means that the transition rate spectrum acquired by using the Fermi golden rule in Eq. (3.34) is valid for the study of the MBL phase.

Total perturbation is $\hat{H}_p = \hat{H}_{p1} + \hat{H}_{p2}$, and the corresponding transition rate spectrum is

$$\mathcal{P}(\omega) = \mathcal{P}_1(\omega) + \mathcal{P}_2(\omega), \tag{4.47}$$

where the first term is given by

$$\mathcal{P}_1(\omega) = \omega_k^2 \mathcal{J}_2^2(\beta) \sum_{if} p_i \frac{\gamma_{if} \left| \langle u_f | \hat{n}_k | u_i \rangle \right|^2}{(\omega_{fi} - 2\omega)^2 - \frac{1}{4}\gamma_{if}^2}, \tag{4.48}$$

and the second part is written as

$$\mathcal{P}_2(\omega) = \sum_{l=k-1}^{k} \frac{J_k^2}{4} \mathcal{J}_2^2(\beta) \sum_{if} p_i \frac{\gamma_{if} \left| \langle u_f | \hat{b}_i^\dagger \hat{b}_{i+1} + \hat{b}_{i+1}^\dagger \hat{b}_i | u_i \rangle \right|^2}{(\omega_{fi} - 2\omega)^2 - \frac{1}{4}\gamma_{if}^2}. \tag{4.49}$$

It can be shown that if $C_{g_i} \ll C_i$, it follows that $\omega_i/J_i \gg 1$. The assumptions we made are valid since the typical values for $\omega_i/(2\pi)$ are between $5 - 10$ GHz and the values for $J_i/(2\pi)$ are around 100 MHz. This means that the transition rates coming from $\mathcal{P}_2(\omega)$ are negligible, and we can approximate

$$\mathcal{P}(\omega) \approx \mathcal{P}_1(\omega) = \mathcal{P}_1(\omega) = \omega_k^2 \mathcal{J}_2^2(\beta) \sum_{if} p_i \frac{\gamma_{if} \left| \langle u_f | \hat{n}_k | u_i \rangle \right|^2}{(\omega_{fi} - 2\omega)^2 - \frac{1}{4}\gamma_{if}^2}. \tag{4.50}$$

Chapter 5

Numerical methods and efficiency

Numerical modelling of a quantum many-body system can be very laborious as the size of the system grows. This is because the Hilbert space grows exponentially as we add more interacting bodies into the system. In our case, we have N transmon qubits with at most M excitations in the system and, thus, the size of the total Hilbert space grows as M^N (the size of the system Hilbert space is diminished because of the conservation of excitations, but the growth is still very rapid).

Our goal is to calculate the transition rate spectra by using Fermi's golden rule. This means that we need to solve every eigenstate and the corresponding eigenenergies for the system in the ergodic phase and in the MBL phase, which ultimately implies that one has to rely on an exact diagonalization method. The diagonalization problem quickly becomes very cumbersome since the dimension of the matrix is determined by the dimension of the Hilbert space.

The nature of the problem, i.e. the Bose-Hubbard model with a hopping interaction between adjacent neighbours, leads to matrices (in Fock basis) which are very sparse. There are already existing algorithms which are specialized to handle such matrices, but it seems that the most of these algorithms are designed and optimized to solve some unique eigenvalues, not the whole spectra (at least in the case of *C++* -libraries). After testing different algorithms from libraries like *Eigen* [66] and *SLEPc* [67–69], it seems that the sparse matrix algorithms do not provide significant speed-up for the diagonalization calculations, although the improvements for memory usage are notable. However, *SLEPc* provides some interesting possibilities for parallel calculations which might prove to be useful if calculations are performed with a supercomputer. In this thesis, we have used the solver for self-adjoint, that is, Hermitian matrices from the *Eigen* library for *C++*.

Rather surprisingly, the eigenvalue problem did not turn out to be the bottleneck of the calculation for the transition rate spectra. The most troublesome part is Eq. (3.34) of Fermi's golden rule. This equation involves two explicit sums, both taken over every eigenstate in the system. In addition, in order to obtain accurate transition rate spectra, one must calculate Eq. (3.34) over many different values of angular frequency of the driving perturbation ω, as well as average over many different disorder realizations. Because of this, the algorithm needs to perform a huge total number of iterations, which ultimately creates the bottleneck. This makes Fermi's golden rule computationally a very hard problem, since the diagonalization in itself is already computationally challenging problem (to obtain the transition rates from Fermi's golden rule, one also needs to perform the diagonalization). Fortunately, these iterations are quite easy to calculate in a parallel manner, which could bring some improvements to the calculation speed.

Chapter 6

Results & Discussion

In this chapter, we present our numerical results and point out some interesting details revealed by these results. The focus of the interpretations is on recognizing the signatures that separates the ergodic phase from the MBL phase. The main results are the transition rate spectra obtained by using Fermi's golden rule which is presented in Eq. (4.50). We form a few sets of spectra where each set shows how the qualitative characteristics of the spectra changes as one parameter is varied. Additionally, we have figures which show how the eigenenergies of the system evolve as the disorder strength W grows. All of these results are obtained by using the Bose-Hubbard model, that is given in Eq. (4.1).

6.1 Transition rate spectra

Here, we approach the spectral properties of the system from a couple of different perspectives, and try to compare the results with the theory that was introduced in chapter 3.

6.1.1 Changing the strength of the disorder

The first approach is to compare the transition rate spectra of the system with different values of the disorder strength W, and observe what significant changes there appears in the spectra when moving from ergodic phase towards the MBL phase. It is assumed that the system has an infinite temperature, that is, the system has an equal probability to be found in any of the energy eigenstates.

The nature of the implementation of disorder is random, and therefore any single realization cannot be trusted to capture the significant properties which are distinctive for the amount of disorder that was used. Thus, we draw multiple disorder realizations corresponding the same value of the disorder strength W. The transition rate spectrum is simulated for each realization and each realization is summed together to form one spectrum. This means that any atypical properties will be overwhelmed by the characteristic behaviour because the probabilities are inclined towards the typical behaviour. This procedure is known as averaging over disorder realizations.

Since our system is one-dimensional transmon chain with external perturbation coupled to one transmon site, we need to take account the fact that driving different sites generally results in a different spectrum. Therefore, we repeat the same procedure with perturbation coupled to different spatial sites as we did with disorder realizations. To be more exact, we simulate the spectra for one disorder realization in which the drive is connected to a different spatial site, and then sum these spectra together to obtain only a single spectrum. This is known as the spatial average.

In figure 6.1 we show a set of spectra in which the disorder strength W is varied between the values 1 - 80 in units of J, while every other parameter is kept fixed. Also, both previously mentioned averaging procedures have been used here. The main purpose for this figure is to find the amount of disorder that is required for the soft gap to appear in the spectrum, since the second signature, that is the gap structure of strong MBL, is not be present in the case of spatial averaging [41] or average over disorder realizations.

It is quite clear that the first spectrum (Fig. 6.1*a*) is in the thermal phase. The spectrum is continuous with vanishing delta-peak structure as expected, but there is a narrow gap at zero frequency. This gap must not be confused with the soft gap since the gap in question is very steep. As the name suggests, the soft gap should behave "softly", that is, $\mathcal{P}(\omega) \sim \omega^{\mu}$ where $\mu > 1$. The steep gap is observed because our system size is very limited system size and very far away from the macroscopic limit, which allows some finite-sized effects to manifest themselves in the simulations which are not predicted by the theory, derived for macroscopic systems. In this case, the system is in the thermal phase which means that the eigenenergies do have level repulsion between each other (see chapter 3), and because of the small size of the system, there are not enough energy levels to make this gap vanish. By increasing the size of the system, it can be seen that the gap gradually fades away [70].

In the second spectrum (Fig. 6.1*b*), there is no recognizable steep gap anymore, which means that the level repulsion between eigenstates is getting weaker as the disorder is increased. However, there are still no signs of the soft gap since the transition rate at zero frequency has clearly the strongest peak.

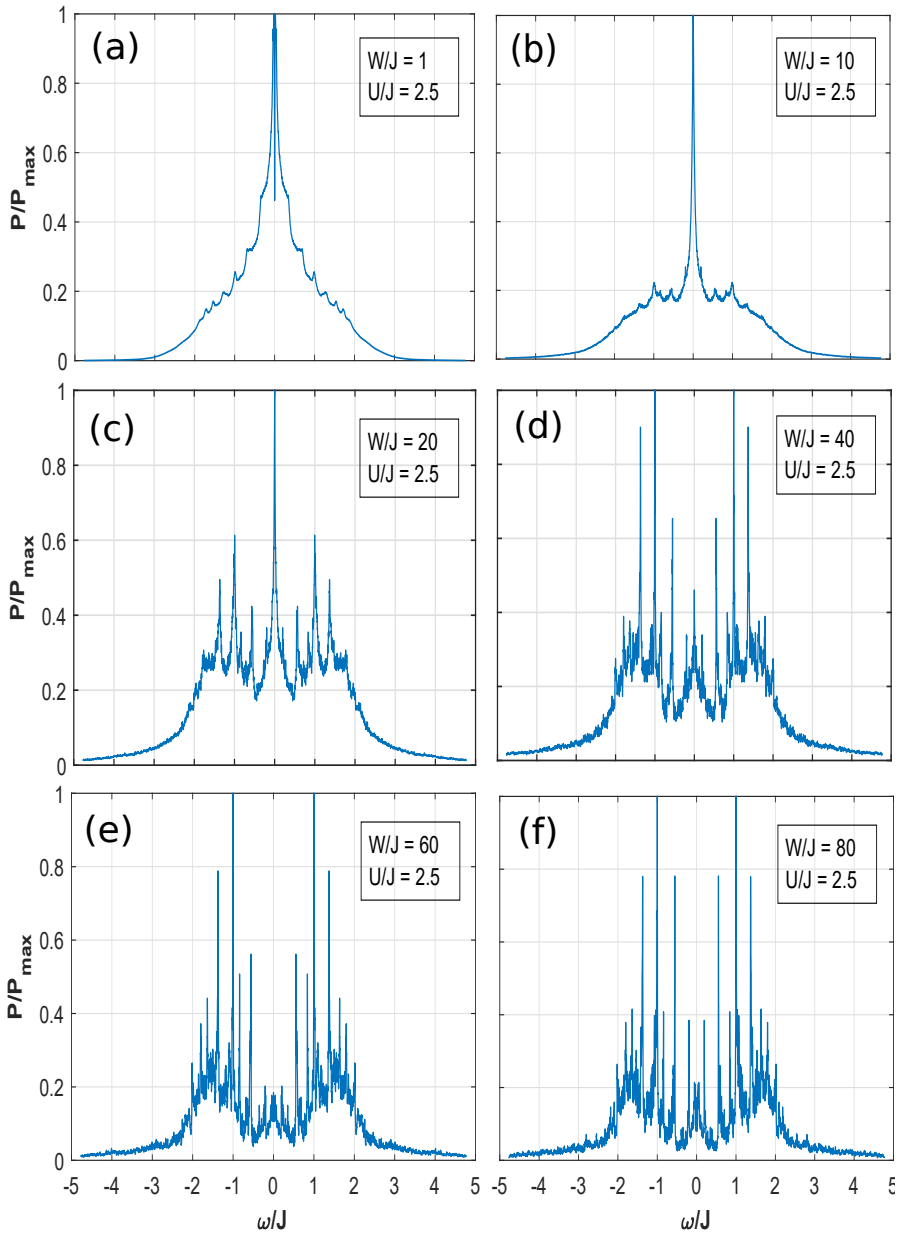

FIGURE 6.1: Transition rate spectra obtained by using Fermi's golden rule. Transition rate P is calculated with Eq. (4.50). Strengths of the peaks are scaled to be relative to the maximum value $P_{\max}$. Size of the system is $N = 8$ and there are $M = 4$ excitations in the system. Number of realizations for each spectra is 500. We have used the same peak width for every transition, that is, $\gamma/(2\pi) = (5/6)$ MHz. The on-site interaction U and the disorder strengths W are declared in the legends.

The rest of the spectra (Fig. 6.1$c-f$) shows that the continuous nature of the thermal phase is starting to deform into a spectrum with the characteristic delta-peak structure as the disorder strength is increased. Surprisingly, there are no clear signs of the soft gap, not even for a disorder strength as large as $W = 80$ (Fig. 6.1f). The soft gap predicted by the theory is absent, but the spectra (Fig. 6.1$c-f$) displays that the relative strengths of the spectral peaks are changing so that the zero-frequency peak is getting weaker and some other peaks are clearly getting stronger as the disorder strength W is increased.

It appears that the peaks in the spectra have some universal characteristics in the sense that they appear even in the case of averaging over many disorder realizations. One interesting characteristic for the higher disorder values is that the largest spectral peak appears at angular frequency $\omega = J$, where J is the strength of the hopping interaction between transmons. One way to understand this for strong disorder is to consider the concept of eigenstates of the local integrals of motion (LIOM), introduced in chapter 2. These eigenstates of the local integrals of motion are slightly distorted versions of the Fock states, which are the eigenstates of the Bose-Hubbard Hamiltonian if the parameters $J_i = 0$ and $U_i = 0$, $\forall i \in \mathbb{N}$. In this case, most of the possible transitions are slightly distorted versions of the transitions in which one excitation moves to a neighbouring site (in Fock basis). This explains why many transitions have energy corresponding to the strength of the hopping interaction J.

6.1.2 Changing the strength of the on-site interaction

In addition to the peak at $\omega = J$, we observe several significant peaks which appear at the same angular frequency value in every spectrum with a large disorder (Fig. 6.1$c-f$). These peaks occur because of the on-site interaction U. On-site interaction makes the peak at $\omega = J$ to divide to several smaller peaks, and the distance between the peaks is determined by the strength of U. This can be clearly seen by comparing the spectra with $U/J = 2.5$ (Fig. 6.1) with another set of spectra with $U/J = 0.4$ (Fig. 6.2). In Fig. 6.2, the strongest peaks are located very close to value $\omega = J$, but in Fig. 6.1 with larger on-site interaction U, the peaks have much larger separation between them. This means that, in general, larger U drives the significant peaks, around $\omega = J$, further away from each other.

In the second set of spectra (Fig. 6.2), we show spectra with different values disorder W, similar to Fig. 6.1, but here we have decreased the relative on-site interaction strength to the value of $U/J = 0.4$. Lower U means that the system resembles more the case of Anderson localization. As we discussed in the previous chapters, in general, any finite

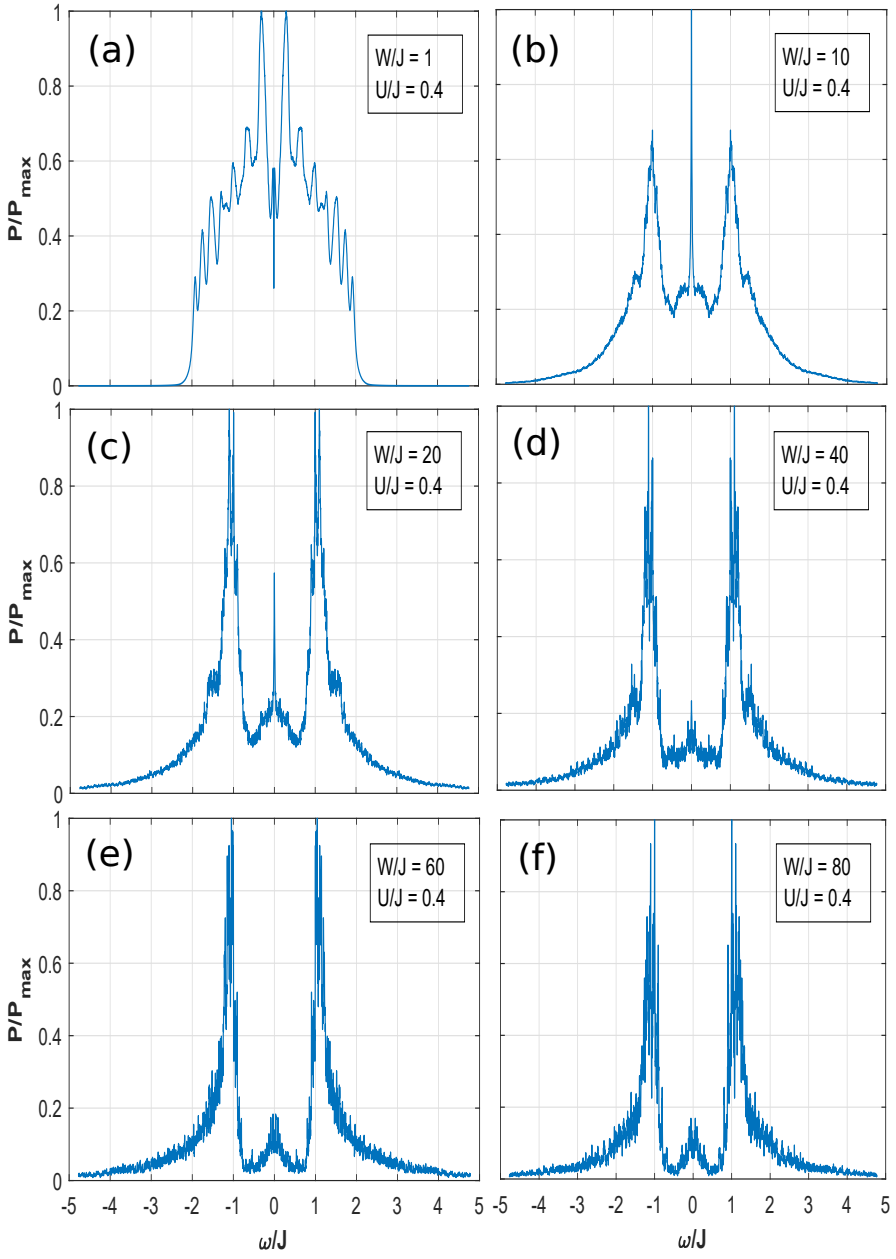

FIGURE 6.2: Transition rate spectra obtained by using Fermi's golden rule. Transition rate P is calculated with Eq. (4.50). Strengths of the peaks are scaled to be relative to the maximum value $P_{\max}$. Size of the system is $N = 8$ and there are $M = 4$ excitations in the system. Number of realizations for each spectra is 500. We have used the same peak width for every transition, that is, $\gamma/(2\pi) = (5/6)$ MHz. The on-site interaction U and the disorder strengths W are declared in the legends.

amount of disorder W is enough to localize the system, therefore the localization in Fig. 6.2 should occur at smaller disorder values compared to Fig. 6.1.

In Fig. 6.2a we can recognize the steep gap, created by level repulsion, which also occurred in Fig. 6.1a. Otherwise, these two spectra are quite different. For $U/J = 0.4$ we show that in comparison to the data with $U/J = 2.5$, the structure has more spectral peaks, and also the relative strength of the zero frequency peak is lower. Both of these signs point towards the conclusion that spectrum 6.2a is more in the direction of the MBL phase.

Another important characteristic, for higher values of disorder strength W (Fig. 6.2 $c - f$), is that for a low value of the on-site interaction U the peaks with significant size are concentrated around $\omega = J$. Also, the gap which resembles the soft gap, appears to be larger and clearer compared to the case with $U/J = 2.5$.

The qualitative differences between the data shown in Fig. 6.1 and in Fig. 6.2, as the disorder is increased, are quite similar. The relative strength of the zero-frequency peak is decreased and, accordingly, those of the other significant peaks are increased, making the appearance of the soft gap more evident.

In Fig. 6.3, we have a set of spectra with the on-site interaction strength $U/J = 5$. In comparison to spectra with $U/J = 2.5$, we observe that there are not any significant qualitative differences. However, there are some detectable differences like the spreading of the spectra. The strongest peaks are getting further away from each other, which ultimately makes it harder to recognize the soft gap. This indeed compliments the fact that it requires more disorder to localize a Bose-Hubbard system with $U/J = 5.0$ compared to the equivalent system with $U/J = 2.5$.

There is an interesting change of behaviour in the transition rate spectra as the on-site interaction U is increased beyond $U/J = 5$. The disorder strength W that is needed to localize the system is decreased. This is opposite if compared to the cases where on-site interaction is less than $U/J = 5$. In Fig. 6.4, we show the transition rate spectra for $U/J = 12.5$ with varied disorder strength. Here we recognize some signs of the progress towards MBL phase. Spectra of Fig. 6.4$d - f$ have much clearer gap between angular frequency values $\omega/J = -1$ and $\omega/J = 1$, and in this sense it resembles more transition rate spectra with $U/J = 0.4$ (Fig. 6.2) than spectra obtained with $U/J = 5.0$ (Fig. 6.3).

The reason why the results do not display the soft gap is not clear. At higher disorder values, one can recognize a soft gap, e.g. if $U/J = 2.5$ it takes place at angular frequency interval $\omega \in [-0.55J,\ 0.55J]$, and the peaks inside this interval could be a side effect from the limited size of the system. However, it is hard to imagine that this would be the only explanation for the case of an intermediate disorder strength (Fig. 6.1c), which

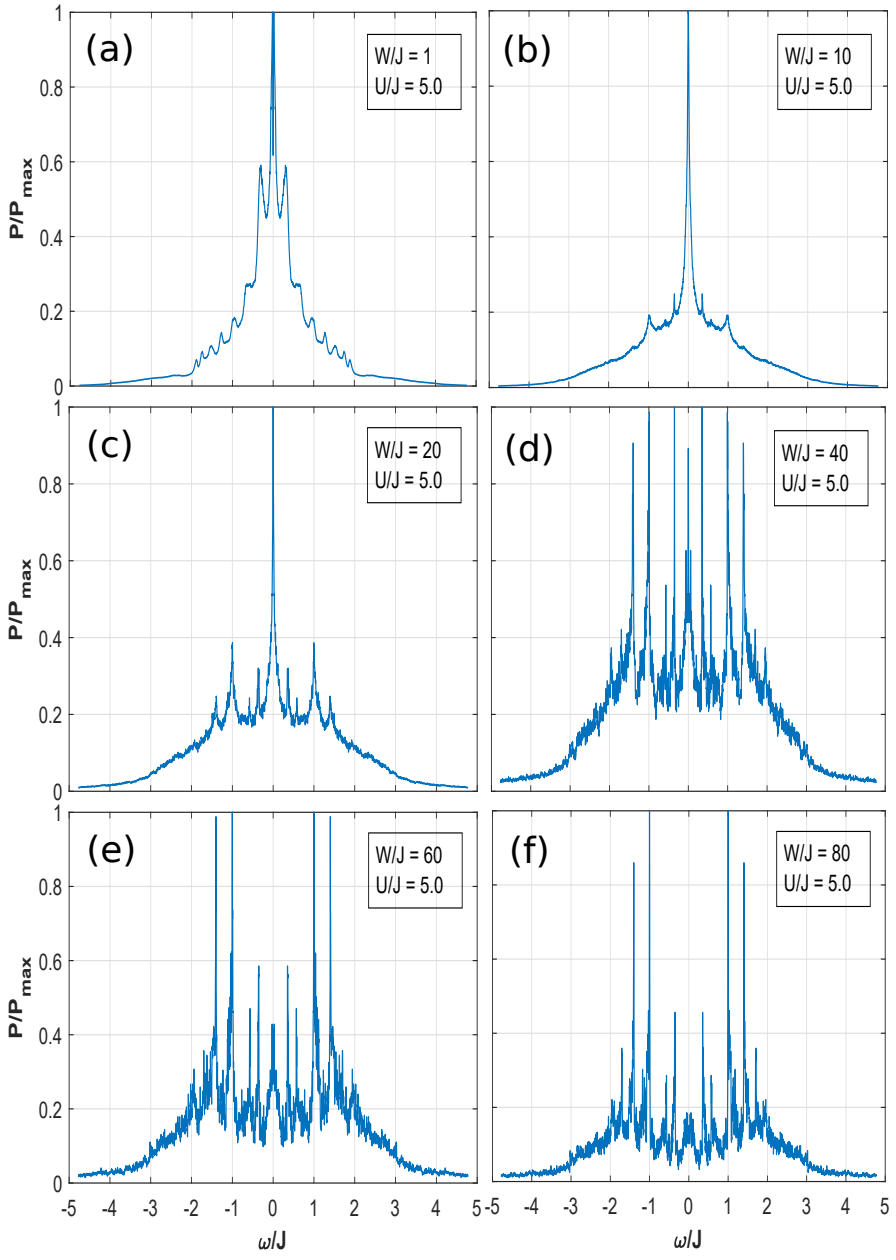

FIGURE 6.3: Transition rate spectra obtained by using Fermi's golden rule. Transition rate P is calculated with Eq. (4.50). Strengths of the peaks are scaled to be relative to the maximum value $P_{\max}$. Size of the system is $N = 8$ and there are $M = 4$ excitations in the system. Number of realizations for each spectra is 500. We have used the same peak width for every transition, that is, $\gamma/(2\pi) = (5/6)$ MHz. The on-site interaction U and the disorder strengths W are declared in the legends.

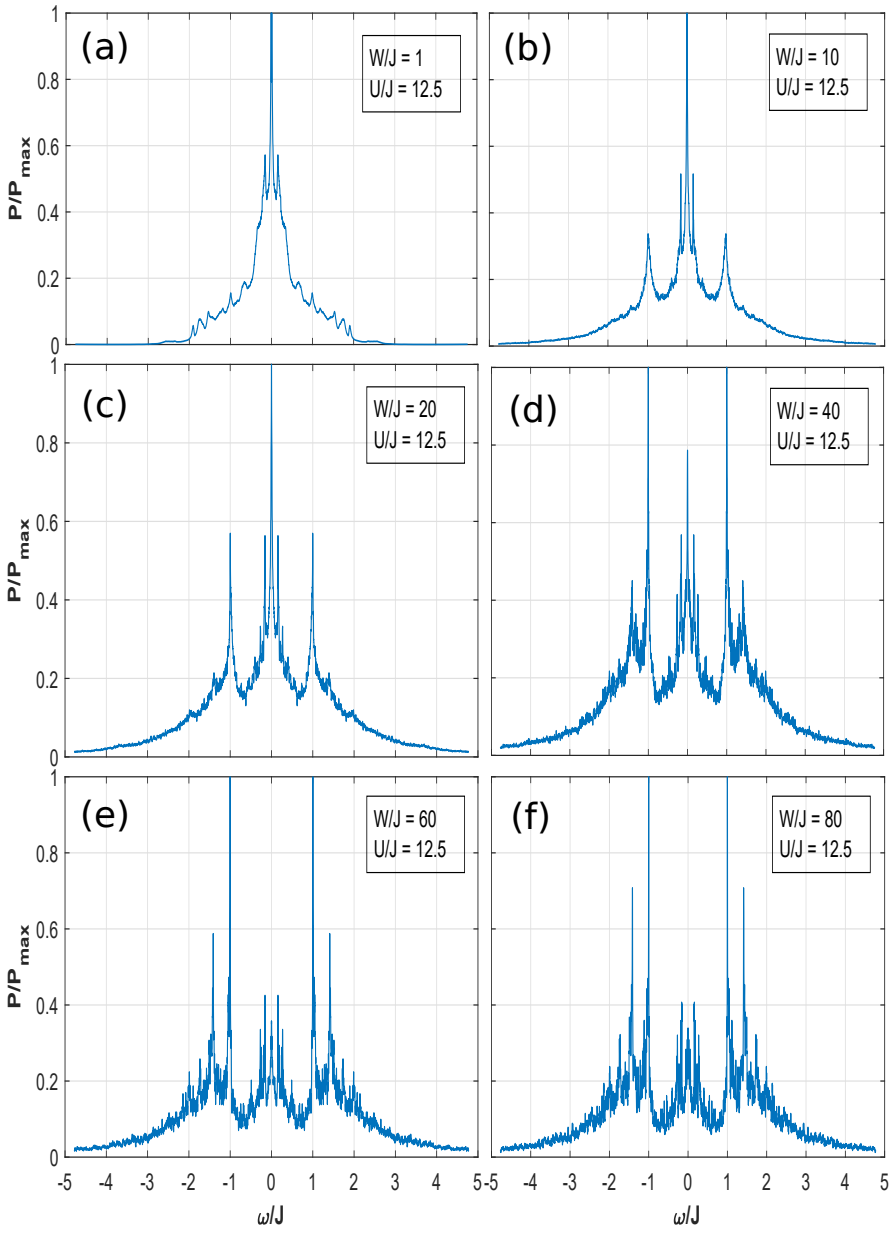

FIGURE 6.4: Transition rate spectra obtained by using Fermi's golden rule. Transition rate P is calculated with Eq. (4.50). Strengths of the peaks are scaled to be relative to the maximum value $P_{\max}$. Size of the system is $N = 8$ and there are $M = 4$ excitations in the system. Number of realizations for each spectra is 500. We have used the same peak width for every transition, that is, $\gamma/(2\pi) = (5/6)$ MHz. The on-site interaction U and the disorder strengths W are declared in the legends.

results in a significant spectral peak at $\omega = 0$. The reason why the limited size of the system should not be an important factor is the fact that the eigenstates are localized, and therefore the most eigenstates do not "feel" the edges of the system. In this case, one contributing factor could be the mobility edge, which means that the eigenstates located outside a certain energy interval are not localized. These thermal eigenstates can contribute to some thermal characteristics of the transition rate spectrum, e.g. the spectral peaks at zero frequency. It is also possible, because of the random nature of disorder realizations, that some disorder realizations form local spatial regions which act as a thermal region inside another region which is in the MBL phase.

6.2 Disorder sweep

Here, we present another spectral method which can be used to distinguish between the ergodic phase and the MBL phase. In this method, the eigenenergies are calculated as a function of the disorder strength W. This demonstrates visually how the level repulsion dominates the behaviour of the eigenenergies for lower disorder values, and how its effect decreases if disorder strength is increased. It is hard to pinpoint the exact disorder value of the transition, but this method can help us to find the approximate disorder region where the behaviour changes from repulsion occurring between energy levels to no repulsion between energy levels. Since the absence of level repulsion is one sign of localization, this method offers us some insight into the localization transition.

In Fig. 6.5, we show the disorder sweep for different values of on-site interaction U. These images only show the behaviour of a small portion of the full energy spectrum. For clearer presentation, we rescale the energy spectra between values 0 and 1, that is, each eigenenergy is scaled according to following formula

$$\epsilon_i = \frac{E_i - E_{\text{min}}}{E_{\text{max}} - E_{\text{min}}}, \tag{6.1}$$

where E_{min} and E_{max} denote the minimum and maximum eigenenergies, and E_i is the i^{th} eigenenergy. To be accurate, in our calculations E_{min} is not the lowest but second lowest energy value. Reason for this is that the lowest energy level tends to separate significantly and, therefore, the presentation of the data is significantly clarified if we use the value for the second lowest level instead.

The plot with a low on-site interaction (Fig. 6.5*a*) clearly shows a behaviour characterized by level repulsion if $W/J \lesssim 5$. As mentioned before, this means that for $W/J \gtrsim 5$, the corresponding eigenstates do not have much spatial overlap between each other.

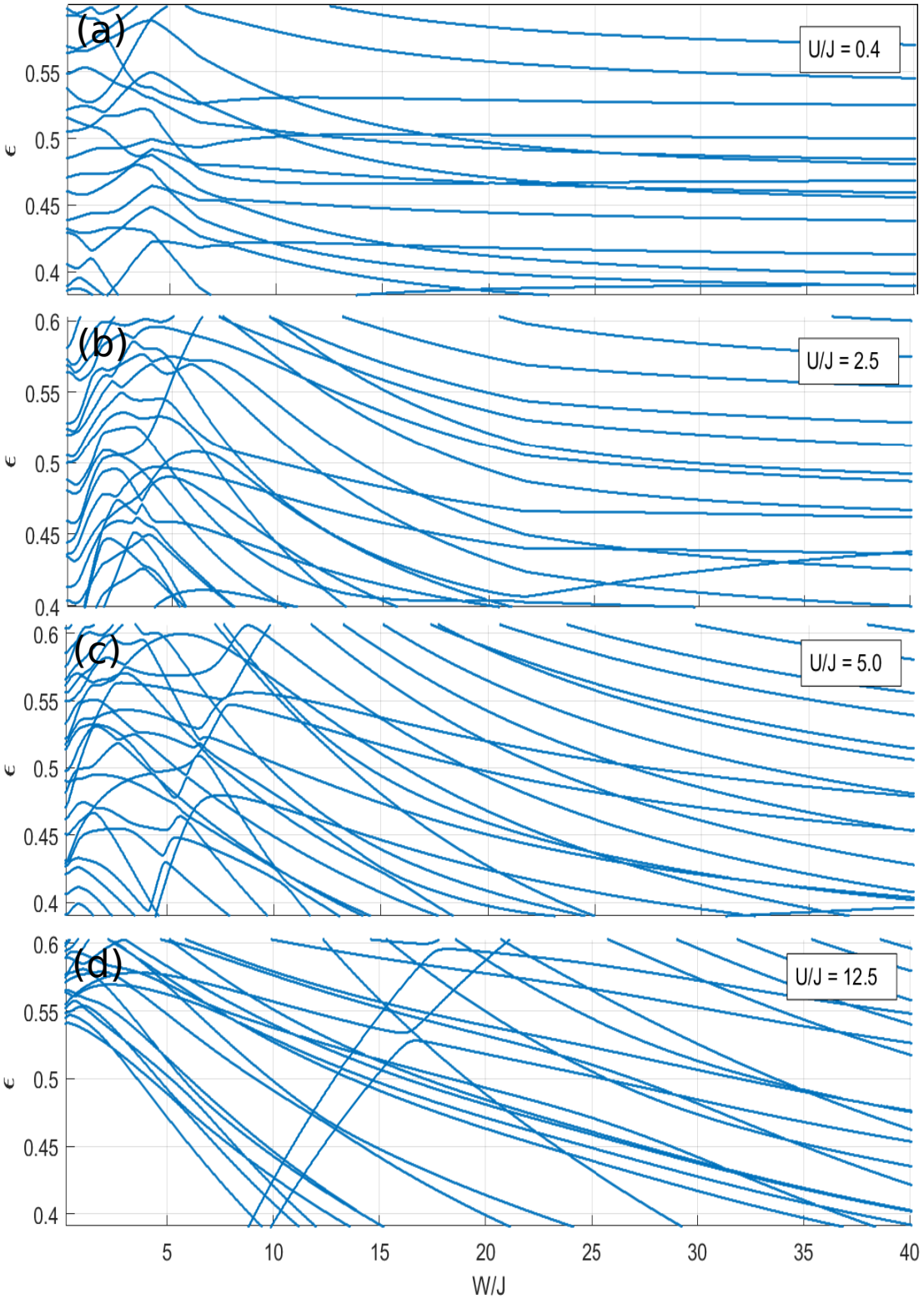

FIGURE 6.5: Behaviour of the eigenenergies as a function of the disorder strength W. Each spectra is calculated for different on-site interaction value U, which are declared in the legend. The size of the simulated system is $N = 6$ with the excitation number $M = 3$. The disorder realization is same in every spectra.

The intermediate on-site interaction strengths are shown in panels b and c of Fig. 6.5. The behaviour is not critically different compared to that is shown in Fig. 6.5a, but it seems that the repulsion between energy levels occurs at slightly stronger disorder values, and ceases around $W/J = 10$.

For very large values of U (Fig. 6.5d), it is hard to see any signs of level repulsion since the energy levels form separate minibands for low disorder and, thus, there are not that many energy levels to repel each other. However, the localization behaviour, that is the absence of level repulsion, should resemble more the system with a small on-site interaction (Fig. 6.5a) than the others.

Chapter 7

Conclusions

We started by studying the basic properties of the many-body localized phase, such as breakdown of eigenstate thermalization hypothesis, emergent integrability in a form of the quasi-local integrals of motion, logarithmic growth of entanglement with respect to time, and area-law entanglement of the many-body localized eigenstates. There are many existing studies regarding these aspects of the many-body localization, but unfortunately, properties like entanglement are not easy to measure in an experimental situation.

To find a method which is more applicable to experiments, we looked into a spectroscopic method which is based on Fermi's golden rule. Based on previous studies, we expected this method to exhibit a spectral "soft" gap which is argued to be a universal property of the many-body localized phase. We presented some arguments which provide an insight into the reasons why the soft gap appears. We also discussed about the spectroscopic method in a more general way, for example, what is the contribution of the interactions regarding the spectra, what is the difference between the weak and strong MBL, and how the dissipation affects the spectrum. We also demonstrated that the absorption spectrum (includes correlation functions explicitly) and Fermi's golden rule transition rate spectrum are equal.

We presented the Hamiltonians for the one-dimensional transmon qubit array and for the Bose-Hubbard model. It was shown that the transmon array Hamiltonian is equal to the Bose-Hubbard Hamiltonian. By using an external magnetic flux as a drive for the transmon array, we showed that the system can be driven without changing the number of excitations in the system.

We shortly discussed the numerical methods related to the calculations. It turned out that if the transition rate spectrum is calculated using Fermi's golden rule, surprisingly, the exact diagonalization of the system Hamiltonian is not the most time-consuming

part. The most expensive part was the summation over every possible initial and final states, and repeating the procedure for many different driving frequencies.

We analyzed the transition rate spectra acquired with Fermi's golden rule. It turned out that the "soft" gap did not clearly appear at the expected disorder values. Instead, we observed a gap-like structure with additional spectral peaks but as the disorder grows the amplitude of these peaks diminish. We also studied how the changing of the strength of the on-site interactions affects the transition rate spectrum. As on-site interactions are increased from zero, the main peaks split into smaller peaks, but maybe somewhat unexpectedly, after the on-site interaction is increased beyond a certain point the peaks seem to merge again. This suggests that if we assume disorder strength W to be constant, the many-body localization is at its strongest if the on-site interactions are small or very strong.

Lastly, we tried another approach to locate and visualize the many-body localization phase transition, by plotting many-body eigenenergies as a function of disorder strength for multiple values of on-site interaction strength. By observing the disorder strength value where the level repulsion vanishes should approximately mark the point where the system enters into the many-body localized phase. It seems, that, in general, it is hard to make any accurate conclusions where the phase transition occurs, but it definitely offers some insight.

The results we presented also raised some questions regarding the spectral peaks. Most interesting and unexpected finding was that some spectral peaks appeared at the zero-frequency in the many-body localized phase. In the future, it would be useful to establish an analytical understanding why these zero-frequency peaks appear, but also a deeper comprehension of the whole spectrum would be important if such spectroscopic experiments are performed in a laboratory. Thus, the results of our work encourages researchers to continue studies to both analytical and experimental directions.

Bibliography

[1] P. W. Anderson, Absence of diffusion in certain random lattices, Phys. Rev. **109**, 5 (1958), URL https://journals.aps.org/pr/abstract/10.1103/PhysRev.109.1492.

[2] D. M. Basko, I. L. Aleiner, and B. L. Altshuler, Metal–insulator transition in a weakly interacting many-electron system with localized single-particle states, Ann. Phys. (N. Y.) **321**, 5 (2006), URL http://www.sciencedirect.com/science/article/pii/S0003491605002630.

[3] I. V. Gornyi, A. D. Mirlin, and D. G. Polyakov, Interacting Electrons in Disordered Wires: Anderson Localization and Low-T Transport, Phys. Rev. Lett. **95**, 20 (2005), URL https://link.aps.org/doi/10.1103/PhysRevLett.95.206603.

[4] V. Oganesyan and D. A. Huse, Localization of interacting fermions at high temperature, Phys. Rev. B **75**, 15 (2007), URL https://link.aps.org/doi/10.1103/PhysRevB.75.155111.

[5] R. P. Feynman, Simulating physics with computers, Int. J. Theor. Phys. **21**, 6-7 (1982), URL https://link.springer.com/article/10.1007/BF02650179.

[6] P. Roushan, C. Neill, J. Tangpanitanon, V. M. Bastidas, A. Megrant, R. Barends, Y. Chen, Z. Chen, B. Chiaro, A. Dunsworth, A. Fowler, B. Foxen, M. Giustina, E. Jeffrey, J. Kelly, E. Lucero, J. Mutus, M. Neeley, C. Quintana, D. Sank, A. Vainsencher, J. Wenner, T. White, H. Neven, D. G. Angelakis, and J. Martinis, Spectroscopic signatures of localization with interacting photons in superconducting qubits, Science **358**, 6367 (2017), URL http://science.sciencemag.org/content/358/6367/1175.

[7] R. L. Weaver, Anderson localization of ultrasound, Wave motion **12**, 2 (1990), URL http://www.sciencedirect.com/science/article/pii/0165212590900342.

[8] R. K. Pathria and P. D. Beale, *Statistical Mechanics*, (Academic Press, Boston, 2011), third edition.

[9] J. Tuorila, Statistical Physics, University of Oulu, lecture notes (2012).

[10] J. P. Sethna, *Statistical Mechanics: Entropy, Order Parameters, and Complexity*, (Oxford Univ. Press, New York, 2006).

[11] L. E. Reichl, *A Modern Course in Statistical Physics*, (Wiley-VCH, Weinheim, 2016).

[12] D. A. Abanin, E. Altman, I. Bloch, and M. Serbyn, Colloquium: Many-body localization, thermalization, and entanglement, Rev. Mod. Phys. **91**, 2 (2019), URL https://link.aps.org/doi/10.1103/RevModPhys.91.021001.

[13] J. J. Sakurai, *Modern Quantum Mechanics*, (Addison-Wesley,, Boston, 1994).

[14] M. Srednicki, The approach to thermal equilibrium in quantized chaotic systems, J. Phys. A **32**, 7 (1999), URL http://stacks.iop.org/0305-4470/32/i=7/a=007.

[15] J. M. Deutsch, Quantum statistical mechanics in a closed system, Phys. Rev. A **43**, 4 (1991), URL https://link.aps.org/doi/10.1103/PhysRevA.43.2046.

[16] M. Srednicki, Chaos and quantum thermalization, Phys. Rev. E **50**, 2 (1994), URL https://link.aps.org/doi/10.1103/PhysRevE.50.888.

[17] M. Rigol, V. Dunjko, and M. Olshanii, Thermalization and its mechanism for generic isolated quantum systems, Nature **452** (2008), URL https://www.nature.com/articles/nature06838.

[18] R. Nandkishore and D. A. Huse, Many-Body Localization and Thermalization in Quantum Statistical Mechanics, Annu. Rev. Condens. Matter Phys. **6**, 1 (2015), URL https://doi.org/10.1146/annurev-conmatphys-031214-014726.

[19] J. Smith, A. Lee, P. Richerme, B. Neyenhuis, P. W. Hess, P. Hauke, M. Heyl, D. A. Huse, and C. Monroe, Many-body localization in a quantum simulator with programmable random disorder, Nat. Phys. **12** (2016), URL https://doi.org/10.1038/nphys3783.

[20] L. Fleishman and P. W. Anderson, Interactions and the Anderson transition, Phys. Rev. B **21**, 6 (1980), URL https://link.aps.org/doi/10.1103/PhysRevB.21.2366.

[21] B. L. Altshuler, Y. Gefen, A. Kamenev, and L. S. Levitov, Quasiparticle Lifetime in a Finite System: A Nonperturbative Approach, Phys. Rev. Lett. **78**, 14 (1997), URL https://link.aps.org/doi/10.1103/PhysRevLett.78.2803.

[22] A. Pal and D. A. Huse, Many-body localization phase transition, Phys. Rev. B **82**, 17 (2010), URL https://link.aps.org/doi/10.1103/PhysRevB.82.174411.

[23] M. Žnidarič, T. Prosen, and P. Prelovšek, Many-body localization in the Heisenberg XXZ magnet in a random field, Phys. Rev. B **77**, 6 (2008), URL https://link.aps.org/doi/10.1103/PhysRevB.77.064426.

[24] J. H. Bardarson, F. Pollmann, and J. E. Moore, Unbounded Growth of Entanglement in Models of Many-Body Localization, Phys. Rev. Lett. **109**, 1 (2012), URL https://link.aps.org/doi/10.1103/PhysRevLett.109.017202.

[25] D. J. Luitz, N. Laflorencie, and F. Alet, Many-body localization edge in the random-field Heisenberg chain, Phys. Rev. B **91**, 8 (2015), URL https://link.aps.org/doi/10.1103/PhysRevB.91.081103.

[26] M. Serbyn, Z. Papić, and D. A. Abanin, Criterion for Many-Body Localization-Delocalization Phase Transition, Phys. Rev. X **5**, 4 (2015), URL https://link.aps.org/doi/10.1103/PhysRevX.5.041047.

[27] D. A. Huse, R. Nandkishore, and V. Oganesyan, Phenomenology of fully many-body-localized systems, Phys. Rev. B **90**, 17 (2014), URL https://link.aps.org/doi/10.1103/PhysRevB.90.174202.

[28] M. Serbyn, Z. Papić, and D. A. Abanin, Local Conservation Laws and the Structure of the Many-Body Localized States, Phys. Rev. Lett. **111**, 12 (2013), URL https://link.aps.org/doi/10.1103/PhysRevLett.111.127201.

[29] J. Z. Imbrie, V. Ros, and A. Scardicchio, Local integrals of motion in many-body localized systems, Ann. Phys. (Berl.) **529**, 7 (2017), URL https://onlinelibrary.wiley.com/doi/abs/10.1002/andp.201600278.

[30] L. Rademaker, M. Ortuño, and A. M. Somoza, Many-body localization from the perspective of Integrals of Motion, Ann. Phys. (Berl.) **529**, 7 (2017), URL https://onlinelibrary.wiley.com/doi/abs/10.1002/andp.201600322.

[31] A. Chandran, I. H. Kim, G. Vidal, and D. A. Abanin, Constructing local integrals of motion in the many-body localized phase, Phys. Rev. B **91**, 8 (2015), URL https://link.aps.org/doi/10.1103/PhysRevB.91.085425.

[32] D. A. Abanin and Z. Papić, Recent progress in many-body localization, Ann. Phys. (Berl.) **529**, 7 (2017), URL https://onlinelibrary.wiley.com/doi/abs/10.1002/andp.201700169.

[33] H. Kim and D. A. Huse, Ballistic Spreading of Entanglement in a Diffusive Nonintegrable System, Phys. Rev. Lett. **111**, 12 (2013), URL https://link.aps.org/doi/10.1103/PhysRevLett.111.127205.

[34] G. Jaeger, *Quantum Information: An Overview*, (Springer, New York, 2007).

[35] M. Serbyn, Z. Papić, and D. A. Abanin, Universal Slow Growth of Entanglement in Interacting Strongly Disordered Systems, Phys. Rev. Lett. **110**, 26 (2013), URL https://link.aps.org/doi/10.1103/PhysRevLett.110.260601.

[36] M. Serbyn, Z. Papić, and D. A. Abanin, Quantum quenches in the many-body localized phase, Phys. Rev. B **90**, 17 (2014), URL https://link.aps.org/doi/10.1103/PhysRevB.90.174302.

[37] E. Thuneberg, Quantum optics in electric circuits, University of Oulu, lecture notes (2017).

[38] M. Serbyn, M. Knap, S. Gopalakrishnan, Z. Papić, N. Y. Yao, C. R. Laumann, D. A. Abanin, M. D. Lukin, and E. A. Demler, Interferometric Probes of Many-Body Localization, Phys. Rev. Lett. **113**, 14 (2014), URL https://link.aps.org/doi/10.1103/PhysRevLett.113.147204.

[39] Y. Bahri, R. Vosk, E. Altman, and A. Vishwanath, Localization and topology protected quantum coherence at the edge of hot matter, Nat. Commun. **6** (2015), URL https://www.nature.com/articles/ncomms8341.

[40] B. Bauer and C. Nayak, Area laws in a many-body localized state and its implications for topological order, J. Stat. Mech.: Theory Exp. **2013**, 9 (2013), URL https://iopscience.iop.org/article/10.1088/1742-5468/2013/09/P09005.

[41] R. Nandkishore, S. Gopalakrishnan, and D. A. Huse, Spectral features of a many-body-localized system weakly coupled to a bath, Phys. Rev. B **90**, 6 (2014), URL https://link.aps.org/doi/10.1103/PhysRevB.90.064203.

[42] S. Johri, R. Nandkishore, and R. N. Bhatt, Many-Body Localization in Imperfectly Isolated Quantum Systems, Phys. Rev. Lett. **114**, 11 (2015), URL https://link.aps.org/doi/10.1103/PhysRevLett.114.117401.

[43] R. Nandkishore, Many-body localization proximity effect, Phys. Rev. B **92**, 24 (2015), URL https://link.aps.org/doi/10.1103/PhysRevB.92.245141.

[44] R. Kubo, M. Toda, and N. Hashitsume, *Statistical Mechanics of Linear Response*, (Springer, Berlin, Heidelberg, 1991).

[45] S. Gopalakrishnan, M. Müller, V. Khemani, M. Knap, E. Demler, and D. A. Huse, Low-frequency conductivity in many-body localized systems, Phys. Rev. B **92**, 10 (2015), URL https://link.aps.org/doi/10.1103/PhysRevB.92.104202.

[46] J. A. Kjäll, Many-body localization and level repulsion, Phys. Rev. B **97**, 3 (2018), URL https://link.aps.org/doi/10.1103/PhysRevB.97.035163.

[47] F. Haake, *Quantum Signatures of Chaos*, (Springer-Verlag, Berlin, Heidelberg, 2006).

[48] M. Silveri, J. Tuorila, M. Kemppainen, and E. Thuneberg, Probe spectroscopy of quasienergy states, Phys. Rev. B **87**, 13 (2013), URL https://link.aps.org/doi/10.1103/PhysRevB.87.134505.

[49] J. Hubbard, Electron Correlations in Narrow Energy Bands, Proc. Royal Soc. A **285** (1965), URL https://royalsocietypublishing.org/doi/abs/10.1098/rspa.1963.0204.

[50] P. Sierant and J. Zakrzewski, Many-body localization of bosons in optical lattices, New J. Phys. **20**, 4 (2018), URL https://iopscience.iop.org/article/10.1088/1367-2630/aabb17.

[51] T. Orell, A. A. Michailidis, M. Serbyn, and M. Silveri, Probing many-body localization phase transition with superconducting circuits (2019), URL https://arxiv.org/abs/1907.04043.

[52] I. Bloch, J. Dalibard, and W. Zwerger, Many-body physics with ultracold gases, Rev. Mod. Phys. **80**, 3 (2008), URL https://link.aps.org/doi/10.1103/RevModPhys.80.885.

[53] J.-y. Choi, S. Hild, J. Zeiher, P. Schauß, A. Rubio-Abadal, T. Yefsah, V. Khemani, D. A. Huse, I. Bloch, and C. Gross, Exploring the many-body localization transition in two dimensions, Science **352**, 6293 (2016), URL https://science.sciencemag.org/content/352/6293/1547.

[54] U. Vool and M. Devoret, Introduction to quantum electromagnetic circuits, Int. J. Circ. Theor. App. **45**, 7 (2017), URL https://onlinelibrary.wiley.com/doi/abs/10.1002/cta.2359.

[55] M. H. Devoret, A. Wallraff, and J. M. Martinis, Superconducting Qubits: A Short Review (2004), URL https://arxiv.org/abs/cond-mat/0411174.

[56] J. M. Gambetta, J. M. Chow, and M. Steffen, Building logical qubits in a superconducting quantum computing system, npj Quantum Inf. **3**, 1 (2017), URL https://doi.org/10.1038/s41534-016-0004-0.

[57] M. H. Devoret and R. J. Schoelkopf, Superconducting Circuits for Quantum Information: An Outlook, Science **339**, 6124 (2013), URL https://science.sciencemag.org/content/339/6124/1169.

[58] J. Koch, T. M. Yu, J. Gambetta, A. A. Houck, D. I. Schuster, J. Majer, A. Blais, M. H. Devoret, S. M. Girvin, and R. J. Schoelkopf, Charge-insensitive qubit design derived from the Cooper pair box, Phys. Rev. A **76**, 4 (2007), URL https://link.aps.org/doi/10.1103/PhysRevA.76.042319.

[59] J. A. Schreier, A. A. Houck, J. Koch, D. I. Schuster, B. R. Johnson, J. M. Chow, J. M. Gambetta, J. Majer, L. Frunzio, M. H. Devoret, S. M. Girvin, and R. J. Schoelkopf, Suppressing charge noise decoherence in superconducting charge qubits, Phys. Rev. B **77**, 18 (2008), URL https://link.aps.org/doi/10.1103/PhysRevB.77.180502.

[60] K. K. Likharev, *Dynamics of Josephson Junctions and Circuits*, (Gordon and Breach, New York, 1986).

[61] M. Dalmonte, S. I. Mirzaei, P. R. Muppalla, D. Marcos, P. Zoller, and G. Kirchmair, Realizing dipolar spin models with arrays of superconducting qubits, Phys. Rev. B **92**, 17 (2015), URL https://link.aps.org/doi/10.1103/PhysRevB.92.174507.

[62] H. Goldstein, C. P. Poole, and J. L. Safko, *Classical Mechanics*, (Addison-Wesley, Boston, 2002).

[63] R. A. Usmani, Inversion of a tridiagonal jacobi matrix, Linear Algebra Its Appl. **212-213** (1994), URL http://www.sciencedirect.com/science/article/pii/0024379594904146.

[64] D. Vion, A. Aassime, A. Cottet, P. Joyez, H. Pothier, C. Urbina, D. Esteve, and M. H. Devoret, *Superconducting quantum bit based on the Cooper pair box*, 173–195 (2011), URL https://link.springer.com/chapter/10.1007/978-94-007-1021-4_7.

[65] M. Abramowitz and I. A. Stegun, *Handbook of Mathematical Functions with Formulas, Graphs, and Mathematical Tables*, (Dover, New York, 1964).

[66] G. Guennebaud, B. Jacob, et al., Eigen v3 (2010), URL http://eigen.tuxfamily.org.

[67] V. Hernandez, J. E. Roman, and V. Vidal, SLEPc: A scalable and flexible toolkit for the solution of eigenvalue problems, ACM Trans. Math. Software **31**, 3 (2005), URL https://dl.acm.org/citation.cfm?doid=1089014.1089019.

[68] V. Hernandez, J. E. Roman, and V. Vidal, SLEPc: Scalable Library for Eigenvalue Problem Computations, Lect. Notes Comput. Sci. **2565** (2003), URL https://link.springer.com/chapter/10.1007%2F3-540-36569-9_25.

[69] J. E. Roman, C. Campos, E. Romero, and A. Tomas, SLEPc Users Manual, Technical Report DSIC-II/24/02 - Revision 3.11, D. Sistemes Informàtics i Computació, Universitat Politècnica de València (2019).

[70] S. Mukerjee, V. Oganesyan, and D. Huse, Statistical theory of transport by strongly interacting lattice fermions, Phys. Rev. B **73**, 3 (2006), URL https://link.aps.org/doi/10.1103/PhysRevB.73.035113.